This article has been published in the Journal of the Mechanical Behavior of Biomedical Materials 2017 Apr; 68:62-79.

Title: Ions-modified nanoparticles affect functional remineralization and energy dissipation through the resin-dentin interface.

Short title: Viscoelasticity at the NPs-modified/resin-dentin interface

Authors: Manuel Toledano[1][*], Raquel Osorio[1], Estrella Osorio[1], LDS, PhD, Antonio Luis Medina-Castillo[2], PhD, Manuel Toledano-Osorio[1], BS, Fátima S. Aguilera[1], LDS, PhD.

Institution: [1]University of Granada, Faculty of Dentistry, Dental Materials Section.

Colegio Máximo de Cartuja s/n

18071 – Granada - Spain.

[2] University of Granada, NanoMyP. Spin-Off Enterprise.

Edificio BIC-Granada. Av. Innovación 1.

18016 - Armilla, Granada, Spain.

*Corresponding author: Prof. Manuel Toledano

University of Granada, Faculty of Dentistry

Dental Materials Section

Colegio Máximo de Cartuja s/n

18071 – Granada - Spain.

Tel.: +34-958243788

Fax: +34-958240809

Email: toledano@ugr.es

ABSTRACT

The aim of this study was to evaluate changes in the mechanical and chemical behavior, and bonding ability at dentin interfaces infiltrated with polymeric nanoparticles (NPs) prior to resin application. Dentin surfaces were treated with 37% phosphoric acid followed by application of an ethanol suspension of NPs, Zn-NPs or Ca-NPs followed by the application of an adhesive, Single Bond (SB). Bonded interfaces were stored for 24 h, submitted to microtensile bond strength test, and evaluated by scanning electron microscopy. After 24 h and 21 d of storage, the whole resin-dentin interface adhesive was evaluated using a Nano-DMA. Complex modulus, storage modulus and tan delta (δ) were assessed. AFM imaging and Raman analysis were performed. Bond strength was not affected by NPs infiltration. After 21 d of storage, tan δ generally decreased at Zn-NPs/resin-dentin interface, and augmented when Ca-NPs or non-doped NPs were used. When both Zn-NPs and Ca-NPs were employed, the storage modulus and complex modulus decreased, though both moduli increased at the adhesive and at peritubular dentin after Zn-NPs infiltration. The phosphate and the carbonate peaks, and carbonate substitution, augmented more at interfaces promoted with Ca-NPs than with Zn-NPs after 21 d of storage, but crystallinity did not differ at created interfaces with both ions-doped NPs. Crosslinking of collagen and the secondary structure of collagen improved with Zn-NPs resin-dentin infiltration. Ca-NPs-resin dentin infiltration produced a favorable dissipation of energy with minimal stress concentration trough the crystalline remineralized resin-dentin interface, causing minor damage at this structure.

Key words: Mechanical, chemical, dentin, adhesive, nanoparticles, mineralization.

1. Introduction

To promote adhesion to dentin, the mineral phase from the substrate has to be removed and the voids left by mineral should be filled with the adhesive resin that undergoes complete *in situ* polymerization to form the hybrid layer (HL) (Nakabayashi and Pashley, 1998). The ideal hybrid layer would be characterized as a three-dimensional collagen-resin biopolymer that provides both a continuous and stable link between the bulk adhesive and dentin substrate (Misra et al., 2004). A volume of demineralized/unprotected collagen remains at the bottom of the hybrid layer (BHL), susceptible of degradation, attributed to the action of host-derived matrix metalloproteinases (MMPs) (Hashimoto et al., 2003; Hebling et al., 2005; Pashley et al., 2004). This jeopardizes the longevity of bonded restorations, compromising the bonding efficacy over time (Breschi et al., 2010; Carrilho et al., 2009). Thus, remineralization of demineralized dentin has important consequences for the improvement of bonding stability.

The ultimate goal in the design and refinement of dental adhesives is to render a stronger and durable adhesion to dental tissues, despite the severe conditions in the oral environment (Profeta, 2014). Dentin adhesives should not only be long-lasting, but promoters of both protection and remineralization of resin-dentin interfaces, triggering the bioactive nature of dentin matrix, by releasing bound bioactive molecules. Minimally invasive dentistry, within the current conservative dental practice is permanently emphasizing on arresting and remineralizing demineralized dentin with either tissue engineering approaches or solution chemical therapy (Toledano and Osorio, 2015). To get ion exchange and mineral precipitation within the hybrid layer, multiple approaches or bioactive materials have been used for functionalization of adhesives and chemical remineralization of dentin, *e.g.*, phosphoproteins, casein

phosphopeptide-amorphous calcium phosphate, bioactive glass particles, colloidal nano-beta-tricalcium phosphate, carboxylic acid-containing polyelectrolytes. All of them claim relative success with respect to the observation of regrowth of minerals at the demineralized dentin. Ceramic bioactive nanospheres, such as hydroxyapatite (HAp) and other engineered nanoparticles (NPs) have also been proposed as a resin filler (Besinis et al., 2014), but they do not possess a controllable release and optimal degradation kinetics (Wu et al., 2011).

In general, minerals elute from the resins, producing a rapid decrease in their chemical-mechanical properties and bond strength (Sauro et al., 2013). At these conditions, ion liberation used to be rapid and not maintained over time. A controllable release and optimal degradation kinetics are crucial but difficult to achieve (Hoppe et al., 2011). Dentin infiltration with polymeric nanoparticles as calcium and phosphate sequestering materials (*i.e.*, carboxylate functionalized polymer particles that bind calcium) previous to the bonding procedure has been proposed (Osorio et al., 2014). These polymers may also act as carriers of other biological factors for the management of tissue mineralization, permitting a controlled ion release rate (Wu et al., 2011). These polymers should bind to collagen and facilitate amorphous calcium and phosphate precursors precipitation, at the hybrid layer. The use of engineered NPs has also become the focus of much research in this field (Besinis et al., 2016).

Zinc has been demonstrated to reduce MMPs-mediated collagen degradation (Osorio et al., 2011), to inhibit dentin demineralization (Takatsuka et al., 2005) and to induce dentin remineralization at the bonded interface (Toledano et al., 2013a). Zinc influences signaling pathways and stimulates a metabolic effect in hard tissue mineralization (Hoppe et al., 2011) and remineralization processes (Barcellos et al., 2016; Lynch et al., 2011). Zinc elicits a specific biological response at the interface of

the material which results in the formation of a bond between tissue and material (Kokubo et al., 1990). The formula for stoichiometric HAp is $Ca_{10}(PO_4)_6(OH)_2$. However, biological apatite is calcium deficient and contains substantial amounts of carbonate. Carbonated apatite is a precursor of HAp, but when it is precipitated in the presence of zinc an exchange between Zn^{2+} and Ca^{2+} occurs *in vitro* forming a substituted apatite compound (Mayer et al., 1994). The binding constant of Zn is 8.7 and that of the calcium is 6.8. An isomorphous substitution can be obtained when Ca^{2+} is replaced by Zn^{2+} into dentin HAp (Vasant and Joshi, 2011). The radii of doped ions of Zn corresponds with 0.074 nm, smaller than Ca, *i.e.*, 0.099 nm; thereby, it is easy for zinc to fill in the vacancy of crystal lattice presenting as lose of certain electrical neutrality (Song et al., 2003). Incorporating zinc into the chemical formulation of resin adhesives increases the potential for intrafibrillar remineralization at partially demineralized collagen matrices (Toledano et al., 2016a).

The degree and the quality of the mineralization will affect the mechanical properties of dentin. Indeed, the extrafibrilar minerals act as a granular material that can withstand load, but in the absence of intrafibrilar mineralization. Intrafibrilar mineralization is the key factor for ensuring that collagen fibrils have the same high modulus of elasticity as occurs in natural biomineralized dentin (Balooch et al., 2008). Therefore, the increase of the elastic modulus of the partially demineralized collagen is directly related to the precipitation of minerals at the resin-dentin interface has (Li et al., 2012), and more specifically at the intrafibrillar compartment (Balooch et al., 2008; Bertassoni et al., 2009). Atomic force microscopy (AFM) nano-indentation is the most commonly applied means of testing the mechanical properties of materials or substrates (Poon et al., 2008), and it was deemed to be a suitable method for the determination of the visco-elasticity of hard tissues (Balooch et al., 2008; Bar-On and Wagner, 2012), at

nanoscale (Hu et al., 2015). Viscoelastic materials, as dentin (Toledano et al., 2015) deform according to a combination of these properties and, as such, exhibit time-dependent strain (Hayot et al., 2012). The complex modulus, as a measure of the resistance of a material to dynamic deformation (Ryou et al., 2013), can be decomposed into storage (elastic) and loss (damping) modulus components (Wilkinson et al., 2015). The storage modulus E' (also called dynamic stiffness) characterizes the ability to store energy by the sample during a cycle of loading (Hayot et al., 2012), which is then available for elastic recoil. The storage modulus is the measure of the sample's elastic behavior. Any resulting phase lag between the force applied and the displacement is related to a loss of energy known as the loss modulus or damping E'' (Hayot et al., 2012). The ratio of the loss to the storage is the tan delta (δ) and is often called damping. Even more, the nano-DMA analysis shows that the dampening (or viscous) behavior of the tissue is much more sensitive to the structural changes that occur with the oral function and than the quasi-static behavior (Ryou et al., 2015). Thereby, it requires the capacity to absorb mechanical shock waves and alleviate stresses at these locations in order to prevent crack propagation across the boundary between the two phases of dentin and thus, may serve as useful biomimetic models for joining mechanically dissimilar biomaterials to restore form and function (Marshall et al., 2001).

Scanning probe microscopes and, in particular AFM have facilitated the imaging and analysis of biological surfaces with little or no sample preparations (Habelitz et al., 2002). AFM operates in a near field with a sharp probe by scanning, enabling characterization of three-dimensional surface morphology with minimal sample preparation and high resolution. AFM has been widely used to visualize the dentin matrix and to determine the spatial relationship between mineral and collagen and their

morphology/topology as well (Hu et al., 2015). By integrating AFM and nano-DMA, both morpho and nanomechanical properties can be obtained. In particular, biological sample systems resemble complex biochemical and biophysic architectures (Rettler et al., 2013).

The vast majority of the research work has been focused on the histological, microscopic and mechanical aspects of dentin, but rarely on the underlying molecular structure which is integral to a full understanding of the adhesive-based therapy, especially its effect on the mineral content and collagen matrix (Liu et al., 2014). Even more, there exist contradictory results that arise from poor characterization of the NPs-loaded biomaterials and their interaction with the target site (Zhao et al., 2016). Active research in this area is helping to build a more solid base in understanding of NPs-tissue interaction. In this respect, Raman is a powerful tool in generating direct information about the molecules of a sample. Thereby, this study was complemented with Raman spectroscopy and cluster analysis, that offers nondestructive measures and provide an insight on biochemical nature and molecular structure, and emission spectroscopies of the tissue. It is used as a quantitative chemical assessment methodology for biological samples in conjunction with the fact that the Raman peak intensity is proportional to the number of molecules within the volume of the scanned area (Milly et al., 2014). Raman mapping, in combination with multivariate data analysis, is a label free imaging method for the analysis of dentin sections. This combined approach yields images depicting a semi-quantitative distribution of the biochemical species in the tissue with high resolution (Bonifacio et al., 2010). Micro-Raman mapping technique appeared to offer a powerful method to directly analyze the resin-dentin interface's constituents and their distribution after placing the restoration. Compared to the conventional histological and microscopic methods Raman spectroscopy and cluster analysis result advantageous

because they are fast, non-intrusive, stain-free, quantitative and less prone to human subjectivity. The combination of various chemometric methods is essential in providing different images conveying complementary information about the tissue, for studying biochemical and morphological changes during resin-dentin interface degradation and remineralization.

The aim of the present study was to infiltrate calcium or zinc-loaded polymeric nanoparticles into phosphoric acid etched dentin, prior to the adhesive application, in order to assess the maintenance in bond strengths and a potential improvement of both chemical and mechanical properties at the short term (21 d), after mineral precipitation at the resin-dentin interface. The null hypotheses to be tested are that calcium and zinc loaded nanoparticles infiltration into etched dentin, (1) does not affect dentin bond strengths, (2) does not influence the dynamic mechanical behavior at the hybrid layer, after 21 days of SBFS storage and, (3) does not facilitate remineralization at the demineralized bonded interface.

2. Material and Methods

2.1. Nanoparticles production

PolymP-*n* Active nanoparticles (NPs) were acquired from NanoMyP (Granada, Spain). Particles are fabricated trough polymerization precipitation. Precipitation polymerization is used to prepare polymeric nanospheres of uniform size and shape free of any added surfactant or stabilizer. This technique starts as a homogeneous mixture of monomer, initiator, and optional solvents, and during the polymerization, the growing polymeric chains are separated from the continuous medium by changes in the mixing free energy (Medina-Castillo et al, 2010). NPs are composed by 2-hydroxyethyl

methacrylate (backbone monomer), ethylene glycol dimethacrylate (cross-linker) and methacrylic acid (functional monomer).

2.2. *Zinc and calcium complexation*

Calcium-doped NPs (Ca-NPs) and Zinc-doped NPs (Zn-NPs) were produced. For zinc and calcium complexation 30 mg of NPs were immersed at room temperature, during 3 days under continuous shaking in 15 ml aqueous solutions of $ZnCl_2$ or $CaCl_2$ (containing zinc or calcium at 40 ppm at pH 6.5), in order to reach the adsorption equilibrium of metal ions. Then, the suspensions were centrifuged and the particles were separated from the supernatant. Attained ion complexation values are 0.96 ± 0.04 µg Ca/mg NPs and 2.15 ± 0.05 µg Zn/mg NPs (Osorio et al., 2016a).

2.3. *Specimen preparation*

Fifty two extracted unerupted human third molars were used. Written informed consent from volunteer donors was obtained, and the research protocol was approved by the Institutional Review Board. Dentin surfaces were obtained after horizontally teeth sectioning below the dentin-enamel junction, specimens were ground flat (180-grit). Before applying Single Bond (SB) resin (3M ESPE, St. Paul, MN, USA), dentin surfaces were phosphoric-acid etched, washed and dried (following manufacturer instructions). An ethanol suspension of NPs, Zn-NPs, Ca-NPs (30 mg/ml) or just an ethanol solution were applied (30 s), in each of the four different experimental groups. Ethanol was evaporated for 30 s and SB resin was applied. A composite build-up was constructed (Tetric EvoCeram, Ivoclar-Vivadent, Schaan, Liechtenstein). The resin-bonding specimens were stored in simulated body fluid solution (SBFS) at 37º C for 24 hours.

2.4. *Microtensile bond strength (MTBS)*

Bonded tooth were sectioned into 1 mm^2 cross-sectioned beams (10 per teeth). Beams were attached to a modified Bencor Multi-T testing apparatus (Danville Engineering Co., Danville, CA, USA) and tested to failure in tension, using a universal testing machine (Instron 4411; Instron Corporation, Canton, MA, USA) at a crosshead speed of 0.5 mm/min. Values were converted to MPa and analyzed by ANOVA and Student-Newman-Keuls multiple comparisons ($p < 0.05$). The employed computer software was SPSS/PC+. To determine the mode of failure, fractured specimens were examined with a stereomicroscope (Olympus SZ-CTV; Olympus, Tokyo, Japan) at 40x magnification. Selected debonded dentin sticks were submitted to critical dried point, carbon covered and analyzed by field emission scanning electron microscopy (FESEM) (Gemini, Carl Zeiss, Oberkochen, Germany).

2.5. *Nano-DMA analysis and Atomic Force Microscopy analysis (AFM) imaging*

Three restored teeth of each group were sectioned in 1 mm thick slabs and were submitted to nano-DMA and AFM analysis at 24 h and 21 d time points, in hydrated conditions (simulated body fluid solution-SBFSS). Property mappings were conducted using a Ti-750D TriboIndenter (Hysitron, Inc., Minneapolis, MN) equipped with nano-DMA III, a commercial nano-DMA package. The nanoindenter tip was calibrated against a fused quartz sample using a quasistatic force setpoint of 5 µN to maintain contact between the tip and the sample surface. A dynamic (oscillatory) force of 5 µN was superimposed on the quasistatic signal at a frequency of 200 Hz. Based on a calibration modulus of the tip value of 1.1400E+3 N/mm^2 for the fused quartz, the best-fit spherical radius approximation for tip was found to be 150 nm, for the selected nano-

DMA scanning parameters. Modulus mapping of our samples was conducted by imposing a quasistatic force setpoint, $F_q = 5$ μN, to which we superimposed a sinusoidal force of amplitude $F_A = 1.8$ μN and frequency $f = 200$ Hz. Data from regions approximately 30x30 μm in size were collected using a scan rate of 0.2 Hz. Each scan resulted in a 256 x 256 pixel data array. Specimens were scanned in the hydrated condition by the application of a layer of ethylene glycol over the specimen surface to prevent water evaporation during the analysis.

Under steady conditions (application of a quasistatic force) the indentation modulus of the tested sample, E, was obtained by application of different models that relate the indentation force, F, and depth, D (Han et al., 2011). Most of these theories assume proportionality between the force and the indentation modulus:

$$F = g(D)E \Rightarrow E = \frac{F}{g(D)}. \qquad (1)$$

Where $g(D)$ is a function on the indentation depth, which depends on the geometry of the probe of the indenter. For example, for a spherical probe, the Hertzian contact theory predicts (Han et al., 2011; Hertz, 1881),

$$g(D) = \frac{4R^{1/2}D^{3/2}}{3(1-v^2)}. \qquad (2)$$

In this equation R is the radius of the spherical probe and v is the Poisson's ratio of the tested sample. As mentioned above, in nano-DMA experiments an oscillatory force is superimposed to a quasistatic force:

$$F = F_q + F_A \sin\left(2\pi f t\right), \qquad\qquad (3)$$

With t being the time. Under this imposed force, the indentation depth takes the following form:

$$D = D_q + D_A \sin\left(2\pi f t - \delta\right). \qquad\qquad (4)$$

This means that the indentation depth also oscillates around a quasistatic value, with the same frequency that the oscillating force and delayed by a phase lag δ. In the limit of $F_A << F_q$ it can be expanded the equation (1) to a first order Taylor approximation, to obtain:

$$F_q + F_A \sin\left(2\pi f t\right) = g(D_q)E + g'(D_q)|E*|D_A \sin\left(2\pi f t - \delta\right). \quad (5)$$

In this equation, g' is the first derivative of g, and $E*$ is the complex dynamic indentation modulus. Now, it can be equaled the time-dependent terms and change the time origin, to write:

$$F_A \sin\left(2\pi f t + \delta\right) = g'(D_q)|E*|D_A \sin\left(2\pi f t\right) \qquad\qquad (6)$$

Now, the oscillating force can be decomposed into two terms, the in-phase term, F', and the out-of-phase term, F'' (Macosko, 1994):

$$
\begin{aligned}
F_A \sin\left(2\pi f t + \delta\right) &= F_A \cos\delta \sin\left(2\pi f t\right) + F_A \sin\delta \cos\left(2\pi f t\right) = \\
&= F_A' \sin\left(2\pi f t\right) + F_A'' \cos\left(2\pi f t\right) = F' + F''
\end{aligned}
\qquad (7)
$$

13

Then, from this decomposition two dynamics moduli can be extracted:

$$E' = |E^*|\cos\delta = \frac{F_A\cos\delta}{g'(D_q)D_A} = \frac{F_A{}'}{g'(D_q)D_A}, \qquad (8)$$

which is the in-phase or storage (elastic) modulus.

$$E'' = |E^*|\sin\delta = \frac{F_A\sin\delta}{g'(D_q)D_A} = \frac{F_A{}''}{g'(D_q)D_A}, \qquad (9)$$

which is the out-of-phase or loss (viscous) modulus. Note the position of the phase lag, δ, in these equations.

As mentioned above, these coefficients are directly related with measured parameters, without any particular assumption, except the consideration of the system consisting of the sample and the instrument tip as a driven simple oscillator under stationary conditions.

Data from the adhesive layer (ADH), hybrid layer (HL) or bottom of hybrid layer (BHL), and either the intertubular dentin (ID) or the peritubular cuff (PD), in the vicinity of the interface were acquired, as represented in the Figure 1. For intertubular dentin, discrete values were taken from locations that were at least 3 μm from a peritubular cuff. For the peritubular cuffs, only single indentations were performed on a cuff due to the limited cuff thickness. Statistical analysis was performed with ANOVA and Student Newman Keuls multiple comparisons tests. $P < 0.05$ was set for significance.

An atomic force microscope (AFM Nanoscope V, Digital Instruments, Veeco Metrology group, Santa Barbara, CA, USA) was employed in this study for surface topography analysis. The imaging process was undertaken inside a wet cell in a fully

hydrated state, using the tapping mode, with a calibrated vertical-engaged piezo-scanner (Digital Instrument, Santa Barbara, CA, USA). A 10 nm radius silicon nitride tip (Veeco) was attached to the end of an oscillating cantilever that came into intermittent contact with the surface at the lowest point of the oscillation. Changes in vertical position of the AFM tip at resonance frequencies near 330 kHz provided the height of the images registered as bright and dark regions. 30 x 30 µm digital images were recorded from each dentin surface, with a slow scan rate (0.1 Hz).

2.6.   *Raman spectroscopy and cluster analysis*

A dispersive Raman spectrometer/microscope (Horiba Scientific Xplora, Villeneuve d´Ascq, France) was used to analyze dentin surfaces, at 24 h and 21 d time points. A near-infrared diode laser spot size of ≈ 0.5µm^2, operating at 785 nm, was employed to measure the Raman signal (100 mW power at sample surface) from 400 to 1,700 cm^{-1} Raman wavenumber. A X100/0.90 NA air objective was handled to focus the laser on the sample and collect the Raman signal. The spectrometer was equipped with a CCD detector (DR-324B-FI-327, Andor Technology LTD, UK). Raman signal was acquired using a 600-lines/mm grating. Chemical mapping of the interfaces were performed. For each specimen two areas 30µm x 30µm area of the interfaces at different sites were mapped using 2 µm spacing at X axis and 1 µm at Y axis, and each spectrum was measured by using 3s acquisition time with 3 accumulations. Baseline correction was always performed after acquisition in order to subtract background; a 5th degree polynomial function was used for that purpose. Chemical mapping was submitted to K-means cluster (KMC) analysis using the multivariate analysis tool (ISys® Horiba), which includes statistical pattern to derive the independent clusters. However, Ward's method was employed to get some sense of the number of clusters and the way they merge from the dendrogram. The aim of a factor analysis lies in the

effective reduction of the dataset dimension while maintaining a maximum of information. This method was used to model the data and to determine spectral variances associated for data differentiation. It resulted in the calculation of a new coordinate system whereby variations of the dataset is described via new axes, principal components (PCs). The K-means clustering is a method of analysis based on a centroid model which aims to partition *n* observations into *k* clusters in which each observation belongs to the cluster with the nearest mean (Almahdy et al., 2012). The natural groups of components (or *data*) based on some similarity and the centroids of a group of *data* sets were found by the clustering algorithm once calculated by the software. To determine cluster membership, this algorithm evaluated the distance between a point and the cluster centroids. The output from a clustering algorithm was basically a statistical description of the cluster centroids with the number of components in each cluster. The biochemical content of each cluster was analyzed using the average cluster spectra. The observed spectra were described at 400-1700 cm^{-1} with 10 complete overlapping Gaussian lines, suggesting homogeneous data for further calculations (Ager et al., 2005).

As the cluster centroids are essentially means of the cluster score for the elements of cluster, the mineral and organic components of the resin-dentin interface were examined for each cluster. A comparison of the spectra that were collected from the specimens which compose each subgroup might indicated complete overlap, suggesting similarity between both measurements. It was hence used for identifying significant spectral differences among distinct substrata. A total of 364 points were performed per map. The number of clusters, four, were chosen according to several issues, such as the dendrogram structure, the false-color maps and the cluster centroid (Bonifacio et al., 2010). Each cluster was assigned to a different color, thus obtaining a

false color-image of the substrate on the basis of similar spectral features. Clusters were created following Ward's technique and the dendrogram was calculated applying four factor spectra or principal components, corresponding with four different components at the resin-dentin interface (red, dentin; blue, hybrid layer; green, bottom of hybrid layer; purple, adhesive). For each point of analysis, all spectra described for each cluster were averaged to obtain the mean cluster spectrum. At this point, the mineral component of dentin was assessed as follows:

Relative presence of mineral:

1. *Phosphate* (960 cm^{-1}) *and carbonate* (1070 cm^{-1}) *peaks and areas of their bands*. Peak heights were processed in absorbance units.

2. *Relative mineral concentration* (MMR) (*i.e.*, mineral-to-matrix ratio): It was inferred from the visible ratio of the intensities of the peaks at 960 cm^{-1} (phosphate) (PO_4^{3-}), MMR_P or at 1070 cm^{-1} (carbonate) (CO_3^{2-}), MMR_C, and CH_2 cm^{-1} (proteins). These indexes concerned with the maximum relative degree of mineralization (Karan et al., 2009; Kunstar et al., 2012; Schwartz et al., 2012).

Crystallinity:

It was evaluated based on the full width at half maximum (FWHM) of the phosphate band at 960 cm^{-1}, $FWHM_P$, and carbonate band at 1070 cm^{-1}, $FWHM_C$. These indexes expressed the crystallographic or relative atomic order, since narrower peaks suggest less structural variation in bond distances and angles (Schwartz et al., 2012). In general, the narrower the spectral peak width is, the higher the degree of mineral crystallinity (Karan et al., 2009).

Gradient in mineral content (GMC), or carbonate content of the mineral crystallites:

It was assessed as the relationship between the ratio of heights at 1070 cm^{-1} (carbonate) (CO$_3^{2-}$) to 960 cm-1 (phosphate) (PO$_4^{3-}$), indicating carbonate substitution for phosphate (Schwartz et al., 2012).

The organic component of dentin was analyzed examining the following parameters:

Normalization: Phenyl group: The peak at 1003 cm^{-1}, which is assigned to C-C bond in the phenyl group, was used for normalization (Xu and Wang, 2011).

Crosslinking:

1. AGEs (advance glycation end products)-pentosidine at 1550 cm^{-1}, interpreted as a marker of the aging process (Sell and Monnier, 1989).

Nature of collagen:

1. Amide III, CH$_2$ and amide I: The peaks at 1246/1270, 1450 and 1655/1667 cm^{-1}, assigned to amide III, CH$_2$ and amide I, respectively, are sensitive to the molecular conformation of the polypeptide chains (Jastrzebska et al., 2003; Xu and Wang, 2011). The decrease of amide I peak indicates damage or removal of collagen fibrils (Xu and Wang, 2012). 1450 cm^{-1} (CH$_2$ deformation bands) is generally assigned to proteins, lipids and carbohydrates; it is in accordance with the immature stage (Vanna et al., 2015).

2. Ratio amide I/amide III concerned the organization of collagen (Xu and Wang, 2012).

3. 1340 cm^{-1} peak: This signal has been assigned to protein α-helices where intensity is sensitive to molecular orientation (Wang et al., 2009).

Degree of adhesive efficacy:

1. *Degree of conversion of adhesive*

Ratio 1637/1608. The peak appearing at 1637 cm^{-1} is associated with C=C of methacrylate, and the peak at 1608 cm-1 is related to C-C in phenyl of adhesive monomer (Xu and Wang, 2012).

2. *Bis-GMA penetration*

Ratio1113/1667. The peak appearing at 1113 cm^{-1} is associated with C-O-C of adhesive, and the peak at 1667 cm^{-1} is related to amide I (Wang and Spencer, 2003; Xu and Wang, 2012).

3. *Adhesive (Bis-GMA and HEMA) penetration*

Ratio 1450/1667. The peak appearing at 1450 cm^{-1} is assigned to the CH$_2$ group of both Bis-GMA and HEMA, and the peak at 1667 cm^{-1} is related to amide I (Wang and Spencer, 2003; Xu and Wang, 2012).

3. Results

Mean MTBS values, standard deviations and modes of failure are reported in Table 1. Attained viscoelastic moduli are displayed in Table 2. Mineral, organic and adhesive components obtained through Raman analysis are found in Tables 3a, 3b, 4 and 5. FESEM images from debonded dentin surfaces are shown in Figure 2. Figure 3 contains scanning DMA analysis of SB resin/24 h and Ca-NPs+resin/24 h groups, and 3-D contour maps of NPs+resin/24 h and Zn-NPs+resin/24 h groups. Figure 4 shows 3-D contour maps of SB resin/21 d and Ca-NPs+resin /21 d groups, and scanning DMA analysis of NPs+resin/21 d and Zn-NPs+resin/21 d groups. Figure 5 contains topographic mapping images obtained by AFM of the resin/dentin interface created using SB resin/24 h, NPs+resin/24 h, Ca-NPs+resin/ 21 d and Zn-NPs+resin/21 d. Figures 6, 7 and 8 contain 2D micro-Raman maps of the phosphate peak intensities, K-

means clustering map and the Raman spectra of principal components of the groups after 21 d SBFS immersion.

Table 1. Mean and standard deviation (SD) of microtensile bond strength (MPa) to dentin and mode of failure of the different experimental groups.

	MTBS Mean (SD)	Mode of failure		
		Adhesive	**Cohesive**	**Mixed**
SB	30.01 (5.31) a	0	0	100
NPs	25.39 (4.65) a	10	0	90
Zn-NPs	27.18 (6.35) a	4	0	96
Ca-NPs	25.03 (7.33) a	7	0	93

Abbreviations. MTBS: microtensile bond strength to dentin. SD: standard deviations. SB: Single Bond. NPs: nanoparticles. Zn-NPs: zinc-loaded nanoparticles. Ca-NPs: calcium-loaded nanoparticles. For each vertical column values with identical letter indicate no significant difference using Student-Newman-Keuls test (p>0.05).

Table 2. Mean and SD of Complex, Loss, Storage Modulus (GPa) and Tan (δ) attained from experimental interfaces after 24h and 21 days of SBFS storage.

	ZONES	SB			NPs			Ca-NPs			Zn-NPs		
		CM (E*) Mean (SD)	SM (E´) Mean (SD)	TAN (δ) Mean (SD)	CM (E*) Mean (SD)	SM (E´) Mean (SD)	TAN (δ) Mean (SD)	CM (E*) Mean (SD)	SM (E´) Mean (SD)	TAN (δ) Mean (SD)	CM (E*) Mean (SD)	SM (E´) Mean (SD)	TAN (δ) Mean (SD)
24h	ADHESIVE	30.71 (4.55) A1a	38.57 (3.10) 1a	0.12 (0.04) A1a	37.38 (11.10) A12a	27.00 (3.65) A1b	0.08 (0.04) A1ab	55.86 (2.48) A1b	57.95 (5.14) A1c	0.04 (0.02) A1b	27.13 (9.72) A1a	23.78 (2.07) A1b	0.20 (0.03) A1c
	HYBRID LAYER	44.66 (16.06) A12a	66.69 (6.63) A2a	0.16 (0.01) A1a	46.67 (9.39) A12a	36.36 (5.37) A2b	0.24 (0.03) A2b	64.34 (6.20) A2a	72.60 (9.51) A1a	0.07 (0.01) A1c	99.28 (7.16) A2b	94.93 (3.17) A2c	0.18 (0.01) A1a
	BOTTOM OF HYBRID LAYER	51.48 (13.71) A12a	69.72 (6.99) A2a	0.19 (0.01) A2a	35.99 (8.47) A1a	34.97 (7.77) A12b	0.28 (0.04) A2b	70.3 (8.05) A2b	106.2 (7.57) A2c	0.12 (0.01) A2c	51.8 (7.55) A2b	99.93 (5.60) A2c	0.19 (0.01) A1a
	INTERTUBULAR DENTIN	65.91 (6.18) A2a	67.54 (7.91) A2a	0.22 (0.01) A3a	46.21 (8.58) A12b	36.71 (10.26) A12b	0.27 (0.03) A2b	116.84 (11.17) A3c	129.78 (14.31) A3c	0.13 (0.02) A2c	54.87 (2.93) A1b	52.97 (1.56) A3d	0.27 (0.02) A2b
	PERITUBULAR DENTIN	126.17 (13.95) A3a	147.17 (16.22) A3a	0.12 (0.02) A1a	54.69 (6.30) A2b	53.50 (6.67) A3b	0.29 (0.04) A2b	215.78 (36.26) A4c	215.74 (23.52) A4c	0.14 (0.02) A2a	179.97 (13.87) A3d	156.50 (23.49) A4a	0.08 (0.02) A3c
21d	ADHESIVE	22.31 (7.56) A1a	18.01 (6.20) B1a	0.25 (0.06) B1a	38.08 (2.97) A1b	38.70 (5.07) B1b	0.27 (0.01) B1a	86.76 (25.94) B13c	68.46 (7.02) A1c	0.07 (0.03) A1b	56.38 (2.68) B1d	59.65 (6.26) B1c	0.47 (0.02) B1c
	HYBRID LAYER	41.50 (7.28) A2a	35.67 (8.90) B2a	0.32 (0.03) B12a	38.08 (2.81) A1a	42.08 (2.75) A1a	0.24 (0.009) A2b	116.16 (23.20) B2b	63.11 (5.10) A1b	0.16 (0.009) B2c	85.39 (7.96) A2b	94.69 (8.40) A2c	0.17 (0.01) A2c
	BOTTOM OF HYBRID LAYER	33.27 (3.13) B2a	31.97 (2.73) B2a	0.35 (0.02) B2a	45.49 (3.57) A2b	43.36 (2.82) A1b	0.24 (0.01) A2b	71.82 (2.82) A1c	70.64 (5.30) B1c	0.17 (0.01) B2c	89.73 (9.86) B2d	92.80 (5.23) A2d	0.25 (0.02) B3b
	INTERTUBULAR DENTIN	30.60 (4.17) B2a	25.73 (5.52) B12a	0.39 (0.03) B2a	76.52 (9.49) B3b	66.18 (12.50) B2b	0.29 (0.02) A3b	65.84 (4.08) B1b	63.76 (35.39) B1b	0.22 (0.01) B3c	96.76 (5.08) B2c	85.88 (3.25) B2c	0.20 (0.01) B4c
	PERITUBULAR DENTIN	57.47 (5.66) B3a	61.05 (9.94) B3a	0.42 (0.07) B2a	70.64 (13.58) A3b	65.55 (13.83) A2a	0.30 (0.01) A3b	98.03 (20.88) B3c	105.05 (3.63) B2b	0.10 (0.01) B1c	116.97 (33.95) B2c	151.00 (22.22) A3c	0.07 (0.02) A5c

Abbreviations: PA: phosphoric acid; SB: Single Bond; NPs: nanoparticles; Ca: Calcium; Zn: Zinc; CM: Complex Modulus, LM: Loss Modulus, SM: Storage Modulus; SD: Standard deviation; SBFS: simulated body fluid solution. Same capital letter indicates no significant difference between 24h and 21days storage groups. Same number indicates no significant differences between different zones within the same adhesive and storage group. Identical lower case letter indicates no significant differences between different adhesive groups. Significance was set at P<0.05.

Table 3a. Raman intensities and ratios of Relative Presence of Mineral components attained from experimental interfaces after storage in SBFS 24h and 21d.

		Relative Presence of Mineral											
		Phosphate [961]						Carbonate [1070]					
		Peak		Area		MMR$_P$		Peak		Area		MMR$_C$	
		24h	**21d**	**24h**	**21d**	**24h**	**21d**	**24h**	**21d**	**24h**	**21d**	**24h**	**21d**
SB	ADH	8.69	5.62	257.19	118.90	1.46	1.08	2.33	1.26	89.90	46.96	0.39	0.24
	HL	16.24	9.07	412.46	230.12	3.76	2.12	2.87	1.62	142.56	93.55	0.66	0.37
	BHL	16.77	19.18	425.93	566.98	4.17	4.61	2.77	3.25	149.17	160.88	0.69	0.78
	Dentin	21.17	20.40	537.72	517.31	5.18	6.23	3.97	3.06	214.00	188.45	0.97	0.93
NPs	ADH	6.35	2.45	188	159.30	1.13	1.12	2.01	1.13	108.18	64.22	0.36	0.52
	HL	18.6	4.58	472.25	135.41	5.00	1.93	2.71	0.99	90.17	34.77	0.73	0.41
	BHL	19.36	26.65	491.47	675.66	5.69	10.57	3.17	3.80	206.56	172.35	0.93	1.51
	Dentin	21.18	24.60	537.84	726.94	4.84	6.11	3.19	3.85	118.33	237.21	0.73	0.95
Ca-NPs	ADH	11.55	12.99	341.31	329.22	1.70	2.19	2.31	2.55	123.88	103.01	0.34	0.43
	HL	21.47	19.97	454.14	506.36	4.92	6.14	2.84	3.19	117.21	144.95	0.65	0.98
	BHL	28.51	---	724.3	---	8.83	---	4.32	---	248.31	---	1.34	---
	Dentin	31.3	36.01	795	913.08	8.87	10.98	3.83	5.47	142.55	181.52	1.08	1.66
Zn-NPs	ADH	9.55	9.54	282.12	281.84	1.57	1.56	1.99	2.20	97.00	111.06	0.33	0.36
	HL	21.78	21.78	552.06	552.28	5.81	5.73	2.75	2.76	113.82	114.17	0.73	0.72
	BHL	31.29	---	793.05	---	14.69	---	3.44	---	128.03	---	1.62	---
	Dentin	32.68	32.70	828.31	828.57	7.89	7.86	4.4	4.38	197.33	210.60	1.06	1.05

Abbreviations: SB: Single Bond; NPs: nanoparticles; Ca: Calcium; Zn: Zinc; ADH: Adhesive; HL: Hybrid layer; BHL: Bottom of hybrid layer; MMR: Mineral/Matrix (CH$_2$) Ratio; SBFS: Simulated body fluid solution. For the mineral components the peaks values had been normalized to the intensity of the symmetric phosphate band near 961 cm^{-1}. Peaks positions are expressed in cm^{-1}.

Table 3b. Crystallinity and GMC ratio of mineral components attained from experimental interfaces after storage in SBFS 24h and 21d.

| | | Crystallinity (FWHM) | | | | GMC Ratio C/P | |
| | | Phosphate FWHM$_P$ | | Carbonate FWHM$_C$ | | | |
		24h	**21d**	**24h**	**21d**	**24h**	**21d**
SB	ADH	22.58	16.13	29.34	28.53	0.27	0.22
	HL	19.36	19.35	38.03	44.37	0.18	0.17
	BHL	19.36	22.58	41.21	37.89	0.17	0.35
	Dentin	19.36	19.35	41.21	47.36	0.19	0.15
NPs	ADH	22.58	50	41.07	43.61	0.32	0.46
	HL	19.35	22.58	25.37	26.84	0.15	0.21
	BHL	19.35	19.35	50.00	34.77	0.16	0.14
	Dentin	19.35	22.57	28.34	47.37	0.15	0.15
Ca-NPs	ADH	22.58	19.34	41.17	30.91	0.20	0.19
	HL	16.13	19.35	31.59	34.85	0.13	0.16
	BHL	19.39	---	44.24	---	0.15	---
	Dentin	19.39	19.35	28.45	25.35	0.12	0.15
Zn-NPs	ADH	22.57	22.57	37.40	38.77	0.21	0.23
	HL	19.35	19.35	31.69	31.69	0.13	0.13
	BHL	19.35	---	28.44	---	0.11	---
	Dentin	19.35	19.35	34.38	36.88	0.13	0.14

Abbreviations: SB: Single Bond; NPs: nanoparticles; Ca: Calcium; Zn: Zinc; ADH: Adhesive; HL: Hybrid layer; BHL: Bottom of hybrid layer; FWHM: Full-width half-maximum. GMC: Gradient in Mineral Content.; SBFS: Simulated body fluid solution. For the mineral components the peaks values had been normalized to the intensity of the symmetric phosphate band near 961 cm^{-1}. Peaks positions are expressed in cm^{-1}.

Table 4. Raman intensities and ratios of organics components attained from experimental interfaces (crosslinking and nature of collagen) after storage in SBFS 24h and 21d.

		Crosslinking		Nature and secondary structure of collagen					
		AGEs-Pentosidine [1550]		CH_2 [1450]		Ratio A-I/ A-III		α-helices [1340]	
		24h	**21d**	**24h**	**21d**	**24h**	**21d**	**24h**	**21d**
SB	HL	2.6	2.94	4.32	4.27	0.57	0.41	3.08	3.53
	BHL	2.25	1.78	4.02	4.16	0.50	0.35	2.72	3.79
	Dentin	2.43	1.95	4.09	3.27	0.44	0.25	3.37	2.82
NPs	HL	3.45	2.37	3.72	2.37	0.60	0.31	4.43	3.12
	BHL	3.11	1.07	3.40	2.52	0.40	-0.01	4.90	1.94
	Dentin	4.67	1.68	4.38	4.02	0.56	0.43	6.02	3.81
Ca-NPs	HL	3.79	3.19	4.36	3.25	0.42	0.20	5.32	3.79
	BHL	3.41	---	3.23	---	1.03	---	5.58	---
	Dentin	3.65	2.88	3.53	3.28	0.37	0.42	4.91	5.43
Zn-NPs	HL	3.62	3.68	3.75	3.80	0.33	0.39	4.50	4.55
	BHL	2.79	---	2.13	---	0.17	---	3.02	---
	Dentin	3.65	3.71	4.14	4.16	0.42	0.44	5.75	5.81

Abbreviations: SB: Single Bond; NPs: nanoparticles; Ca: Calcium; Zn: Zinc; HL: Hybrid layer; BHL: Bottom of hybrid layer; A: amide; AGEs: advanced glycation end products; SBFS: Simulated body fluid solution. For the organics components the peaks values had been normalized to the intensity of the pyridinium band near 1032 cm^{-1}. Peaks positions are expressed in cm^{-1}.

Table 5. Raman intensities ratios of adhesive components attained from experimental interfaces after storage in SBFS 24h and 21d.

		Adhesive					
		DC [1637/1608]		Bis-GMA Penetration [1113/A-I]		Adhesive Penetration [1453/1667]	
		24h	**21d**	**24h**	**21d**	**24h**	**21d**
SB	ADH	0.50	0.46	1.62	1.46	1.93	2.13
	HL	0.67	0.39	0.92	1.34	1.20	2.07
	BHL	0.76	0.63	6.31	1.42	1.33	2.10
	ADH	0.40	0.25	1.84	1.40	2.05	3.74
NPs	HL	0.70	0.53	0.81	1.36	1.16	1.85
	BHL	0.47	2.54	1.39	0.57	1.57	6.14
	ADH	0.35	0.09	2.26	1.26	2.50	59.3
Ca-NPs	HL	0.55	0.09	1.32	1.37	1.57	3.21
	BHL	1.38	---	6.31	---	0.45	---
	ADH	0.19	0.19	3.68	1.20	4.73	5.44
Zn-NPs	HL	0.51	0.45	1.16	1.13	1.95	1.94
	BHL	0.02	---	1.99	---	2.88	---

Abbreviations: SB: Single Bond; NPs: nanoparticles; Ca: Calcium; Zn: Zinc ADH: Adhesive; HL: Hybrid layer; BHL: Bottom of hybrid layer; DC: Degree of conversion of adhesive; Bis-GMA: bisphenol A diglycidyl methacrylate; A-I: Amide I; SBFS: Simulated body fluid solution. For the adhesive components the peaks values had been normalized to the intensity of the pyridinium band near 1032 cm^{-1}. Peaks positions are expressed in cm^{-1}.

3.1. Microtensile bond strength (MTBS)

Mean MTBS values, standard deviations and modes of failure are reported in Table 1. Mean MTBS values ranged from ~25 to ~30 MPa and no differences were found between groups. FESEM images from debonded dentin surfaces are shown in Figure 2. Failure after SB application mostly occurred at the bottom of the hybrid layer, where mineral depleted collagen is detected; some resin tags are partially blocking the dentin tubules (Figure 2A). In the group in which non-doped NPs where applied, NPs were found embedded at the hybrid layer, and were homogeneously distributed onto the dentin surface. NPs did not agglomerate and passed through the dentinal tubules (Figure 2B). In Ca-NPs group, mineralization at the hybrid layer was evidenced, being difficult to find demineralized collagen fibers or open tubules (Figures 2C and 2D). Zn-NPs seem to promote tubular occlusion, but collagen fibers were patent at the bottom of the hybrid layer (Figures 2E and 2F). NPs were hardly distinguished.

3.2. Nano-DMA analysis and Atomic Force Microscopy analysis (AFM) imaging

Specimens bonded with SB and tested at 21 d of SBFS storage attained lower complex modulus (E^*) at the bottom of the hybrid layer and dentin (inter and peritubular) that at 24 h. The property map of this resin adhesive-dentin interface after 24 h of storage identified the highest resistance to dynamic deformation, E^*, located at the peritubular areas (Figure 3A). The greatest discrepant values were encountered between peritubular and intertubular dentin (Table 2). The 3-D contour map analysis reflects the diminished complex modulus after 21 d of SBFS storage, which affects the whole resin-dentin interface (Figure 4 A). Proportional discrepancies among the different structures, at the interface, remain. Tan δ increased and the storage modulus (E') decreased at the whole interface after 21 d of immersion, indicating lower stiffness

at this time point. In general, both intertubular and peritubular dentin attained lower E^* and E', and higher tan δ at 21 d than at 24 h.

Intertubular dentin of specimens treated with non-doped NPs achieved higher E^* and E' at 21 d than at 24 h of study. The dissimilar dynamic mechanical behavior shown between both dentin structures (intertubular and peritubular dentin) (Table 2) indicates the presence of stress concentration at this location. The 3-D contour map analysis of the storage modulus (E') corresponding to this group (NPs/24 h) unveils the highest elastic behavior attained by the peritubular dentin in the context of this resin-dentin interface (Figure 3B). The hybrid layer and the bottom of the hybrid layer performed similar, after the nano-DMA analysis, when both study periods were compared (Table 2). The tan δ of the hybrid layer was not affected after 21 d of immersion.

Both intertubular and peritubular dentin of specimens treated with Ca-NPs achieved lower E^* and E' at 21 d than at 24 h time point (Table 2). This indicates a reduced resistance to dynamic deformation, and a lower elastic behavior, respectively, at these structures. Specimens treated with Ca-NPs and stored 24 h, showed areas of higher elastic behavior (E') in the property map at peritubular dentin (~216 GPa) (Figure 3C), labelling ~1.85 fold superior E' than at intertubular dentin. This potential zone of stress concentration diminishes after 21 d of immersion, as the complex modulus decreases ~1.5 fold between peritubular and intertubular dentin (Table 2). On the contrary, tan δ exhibited an increased trend at the hybrid layer, the bottom of the hybrid layer and intertubular dentin after 21 d of immersion, but peritubular dentin decreased ~1.4 fold at this time point (Table 2). Advanced processes of intertubular and peritubular mineralization were produced (Figure 5C).

When specimens treated with Zn-NPs were analyzed, both E^* and E' of intertubular dentin increased, but E^* decreased at peritubular dentin after 21 d of

immersion in SBFS (Table 2). Nevertheless, the potential for the stress concentration between peritubular and intertubular dentin, both remineralized (Figure 5D), did also decrease as differences of those viscoelastic properties diminished at these locations after 21 d of storage (Table 2). Tan δ decreased at intertubular dentin, at this time point, indicating greater proportion of energy available for recoil or failure. Tan δ values at 24 h of storage clearly demonstrates the stress concentration that generated the highest discrepancy between the peritubular dentin and the rest of components involved in the resin-dentin interface (Figure 3D). Tan δ at the bottom of the hybrid layer increased ~1.32 fold after 21 d of SBFS storage, in comparison with 24 h time point.

Samples treated with both Ca-NPs and Zn-NPs achieved the highest E^* at the peritubular dentin, after 21 d of immersion, though at 24 h, Ca-NPs obtained the highest values of E^* at this location. Specimens infiltrated with Zn-NPs attained the maximum E^* at intertubular dentin. These results were higher than those obtained in specimens that were just treated with SB after 21 d of immersion (~3.16 and ~2.04 fold at intertubular and peritubular dentin, respectively) (Figure 4A). Samples infiltrated with Zn-NPs showed the greatest values of E' at intertubular and peritubular dentin after 21 d of storage, but samples treated with Ca-NPs obtained the highest values at these locations after 24 h of storage. The storage modulus map (Figure 3C) shows the colored viscoelastic profiles of both structures, ranging from 215.74 GPa (peritubular dentin) up to 129.78 GPa (intertubular dentin) (Table 2). The lowest tan δ values, at peritubular and intertubular dentin, were achieved in dentin samples treated with Zn-NPs, at 21 of storage (0.07 GPa) (Figure 4D), and at intertubular dentin, at 24 h of immersion (0.13 GPa) (Figure 3D) (Table 2). Both hybrid layer and bottom of hybrid layer attained the minimum values of tan δ when specimens were infiltrated with Ca-NPs, at 24 h (0.07

and 0.12 GPa, respectively) and 21 d (0.16 and 0.17 GPa, respectively) (Figure 4C) of immersion (Table 2).

3.3.   *Raman spectroscopy and cluster analysis*

Results from Raman analysis are presented in Figures 6, 7 and 8. A map of phosphate peak (961 cm^{-1}) intensities, a color representation of the cluster analysis corresponding to the same mapping zone and *spectra* of principal components are provided for each group. Multivariate maps were displayed in the mode "overlay" and "true colors" of resin-dentin interfaces promoted with SB resin (Figure 6A), Ca-NPs (Figure 7A) and Zn-NPs (Figure 8A) stored in SBFS for 21 d. On the other hand, the cluster analysis displayed for SB specimens, Ca-NPs and Zn-NPs infiltrated interfaces stored for 21 d are illustrated in Figures 6B, 7B, and 8B, respectively. The regions are identified by observation of the cluster centroid *spectra* shown in the same figure. Centroids denote the center of mean of the clusters. Different regions have different cluster. Hierarchical cluster analysis (HCA), from each interface, was obtained and reflected following the ensuing cluster image. HCA decomposed the *data* set into smaller set of linear independent or loading vectors (Toledano et al., 2013b), principal components (PCs), with a corresponding set of score values.

In samples just treated with SB, Ca-NPs and Zn-NPs, as a function of position across the adhesive/dentin interface, the resulting images are shown in Figures 6C, 7C and 8C respectively, and correspond with the different classes location *spectra* or principal components (PCs), that resulted labeled in the differentiated broad zones of major components, as 1) adhesive (ADH) (purple and yellow), *i.e*, adhesive zone with SB in phosphoric acid-conditioned dentin. Figures 7 and 8 show two spectra for the adhesive; mean values between both are registered at the Tables 3a and 3b. 2) hybrid layer (HL) (blue), *i.e*, interface zone where the adhesive and collagen fibers have

intermingled, 3) demineralized dentin at the bottom of the hybrid layer (BHL) (green in Figure 6C, absent in Figures 7C and 8C), *i.e*, partially demineralized dentin with lesser adhesive penetration or even no penetration, and 4) mineral dentin (DEN) (red in Figure 6C, red and green in Figures 7C and 8C), *i.e.* intertubular and peritubular dentin. At Figures 7 and 8 it may be observed that two clusters of dentin were generated; mean values between both are registered at the Tables 3a and 3b.

After 24 h of immersion in SBFS, infiltration of dentin with non-doped NPs, promoted an increase of mineralization at the resin-dentin interface, as the phosphate peak, area, and the mineral to matrix ratio (MMRp) at 960 cm^{-1} increased in all cases, in comparison with the SB group (Table 3a). After 21 d of SBFS storage, specimens treated with non-doped NPs increased their height of the phosphate peaks at the bottom of the hybrid layer and at dentin, in comparison with, *i)* samples infiltrated with NPs immersed for 24 h, and *ii)* samples infiltrated just with SB and kept in SBFS for 21 d (Table 3a).

Specimens treated with Zn-NPs achieved the highest peak and biggest area of the phosphate group, at 24 h of SBFS storage. Ca-NPs attained the highest phosphate peak, the biggest area of the phosphate group and greatest MMR$_P$, in general, after 21 d of SBFS storage. The full width at half maximum (FWHM$_P$) of the phosphate band at 960 cm^{-1} decreased when NPs were or not doped with Zn, at the whole interface and, thereby, crystallinity increased, after 24 h of SBFS storage. Specimens treated with non-doped NPs and stored 21 d decreased the crystallinity at the whole interface, meanwhile specimens treated with Zn-NPs did not change their FWHM$_P$. After 24 h of immersion, crystallinity at the interface of specimens treated with Ca-NPs did not change in comparison with the SB specimens, except at the hybrid layer, where an increase was produced (Table 3b). Samples treated with Ca-NPs and stored 21 d increased their

crystallinity, except at the hybrid layer, when compared with the group of 24 h (Table 3b). Infiltrating the adhesive with non-doped NPs or Ca-NPs, promoted a decrease of the carbonate peak height (1070 cm^{-1}) and area at the hybrid layer of the resin-dentin interface, and at the dentin, in comparison with the SB group, after 24 h of SBFS storage. When samples were stored for 21 d, the hybrid layer of specimens treated with NPs attained a decrease of the carbonate peak. This peak height was higher at the whole interface after infiltrating the dentin with Ca-NPs (Table 3a). In general, MMR$_C$ concerning the carbonate group was higher when NPs were used, at the whole interface after 21 d of immersion, but samples treated with Zn-NPs presented a lower MMR$_C$ at the hybrid layer and at dentin after 21 d. In general, crystallinity of carbonate augmented (lower FWHM$_C$) when NPs were present at the interface, in comparison with samples treated with SB adhesive, except at the bottom of the hybrid layer of samples treated with NPs doped or not with Ca, at 24 h of storage. On the other hand, crystallinity augmented in general, when specimens were treated with Ca-NPs and kept in SBFS for 21 d (Table 3b). The carbonate content of the mineral crystallites, at the hybrid layer, diminished when NPs (doped or not) were employed, in comparison with the SB bonded interfaces (Table 3b), at 24 h of storage. After 21 d, the gradient of mineral content slightly increased at the hybrid layer and at dentin. The carbonate content of the mineral crystallites decreased when NPs, in general, were infiltrated into etched dentin (Table 3b).

After 24 h of immersion in SBFS, crosslinking of collagen increased when NPs (doped or not) were infiltrated into etched dentin before adhesive application. On the other hand, the presence of NPs at the interface promoted a decrease of crosslinking after 21 d of SBFS storage, except when Zn-NPs were used which produced a generalized increase in AGES-pentosidine. The highest intensity peak of AGEs-

pentosidine was achieved at the resin-dentin interfaces infiltrated with Ca-NPs at 24 h time point, and at the dentin substrate of specimens infiltrated with Zn-NPs at 21 d time point (Table 4). On the other hand, the molecular conformation of the polypeptide chains (CH_2) and the organization of collagen (ratio amide I/amide III) followed and irregular trend, as both indexes decreased, in general in the group of dentin infiltrated with Zn-NPs. These indexes augmented at the hybrid layer in the case of dentin treated with Ca-NPs, in comparison with the group of SB, at 24 h of storage time. After 21 d of immersion, peak intensities of CH_2 and ratio amides I/III augmented in specimens infiltrated with Zn-NPs but diminished when Ca-NPs were used (Table 4). The peak corresponding to the molecular orientation of collagen (1340 cm^{-1}) raised when non-loaded NPs were applied, in comparison with the SB group, at 24 h of SBFS immersion. Samples treated with non-doped NPs decreased their molecular orientation after 21 d of storage, in comparison with 24 h. At the hybrid layer, specimens infiltrated with Ca-NPs achieved the highest α-helices intensity that decreased after 21 of SBFS immersion. Specimens treated with Zn-NPs attained the highest peak, at dentin after 21 d of SBFS storage (Table 4). Raman intensities corresponding to the mineral and organic components at the bottom of the hybrid layer was not registered in specimens infiltrated with Ca-NPs or Zn-NPs, and stored 21 d in SBFS, as this structure was not present in the cluster analysis.

After 24 h of immersion in SBFS, the degree of conversion of the adhesive only increased at the hybrid layer of samples treated with non-doped NPs and Ca-NPs, respectively. On the other hand, the Bis-GMA penetration was higher at the hybrid layer of specimens infiltrated with Zn and Ca-doped NPs, at 24 h. After 21 d of storage, Bis-GMA penetration raised at the hybrid layer when dentin was infiltrated with Ca-NPs.

The adhesive penetration augmented, in general, in dentin specimens treated with both Zn and Ca-doped NPs, and decreased when non-doped NPs were applied (Table 6).

4. Discussion

Our results confirm that dentin infiltration with Ca-NPs before the adhesive application provoked a favorable dissipation of energy with minimal stress concentration trough the crystalline remineralized resin-dentin interface.

Infiltration of dentin with NPs did not exert changes in bond strength and the highest percentage of mixed failures among the tested groups (Table 1). When NPs were not applied, the failure existed at the bottom of the hybrid layer, where resin-uncovered collagen was present and a great amount of dentinal tubules were empty. Some dentin collagen fibrils, partially demineralized, exhibited the typical 67 nm periodicity banding, demonstrating diameters below 100 nm, and some fibrils appeared partially fractured at the dentin surface (Figure 2A). This poor Bis-GMA and adhesive penetration through the partially demineralized dentin was confirmed with AFM (Figures 5A, 5B) and Raman analysis (Table 5). The presence of this poorly resin infiltrated layer may lead to MMPs-mediated collagen degradation.[16] A decrease of the relative presence of minerals, crystallinity and carbonate substitution (Tables 3a, 3b), and so the altered organic components (Table 4) is also contributing to this advanced state of degraded interface (Toledano et al., 2016b).

When non-doped NPs were applied previous to the resin infiltration, the highest percentage of adhesive failures were achieved (Table 1) and the demineralized collagen fibrils also exhibited the characteristic periodical striation, with fibrils not denatured or fractured. This failure primarily accounted where demineralized collagen fibrils were

exposed and the resin failed to envelop the collagen network, properly (Prati et al., 1999; Toledano et al., 2006). The increase in the percentage of adhesive failures may be interpreted as a result of the strengthening of the resin-dentin interface from remineralization (Toledano et al., 2016a). Moreover, fibrils had a high width (100 to 200 nm), which usually occurs when intrafibrillar mineralization exists or cross-linking is maintained (Bertassoni et al., 2010; Misra et al., 2004). In general terms, phosphate and carbonate peak heights and areas increased at the interface when NPs were used for dentin infiltration, but peaks and ratios concerning the organic components (crosslinking and nature/secondary structure of collagen) decreased after 21 d of immersion (Tables 3 and 4). Tested NPs had a higher diameter than the width of the collagen interfibrillar spaces, preventing NPs from passing into the hybrid layer (Besinis et al., 2012). However, when smaller particles (20 nm or less) are applied, infiltrative capability into the demineralized dentin is also reduced, due to particle agglomeration and/or to particle binding to demineralized collagen fibres (Besinis et al., 2012). Particle binding to demineralized collagen was produced (Figure 2B). It may be accounted for: 1) the result of the high affinity between the negatively charged polymeric NPs (-43.3 mV) and the positively charged demineralized dentin collagen (Besinis et al., 2012), or 2) due to the binding of COO^- groups from NPs to NH^+ sites at dentin collagen. This step is crucial, as NPs collagen binding is necessary to exert a remineralization effect (Besinis et al., 2012, 2014).

The first null hypotheses to be tested was that calcium and zinc loaded nanoparticles infiltration, into etched dentin, did not affect dentin bond strengths at the hybrid layer has been accepted, as bond strength values does not differ among groups (Table 1). On the other hand, when Ca-NPs were applied, 93% of failures were mixed (Table 1), and surfaces appeared totally covered by mineral deposits in *strata*, primarily

at intertubular dentin, though peritubular and intratubular locations resulted also strongly mineralized. Enhanced bioactivity of Ca-NPs was evident on debonded specimens, as in these dentin surfaces was not possible to observe demineralized collagen or open dentinal tubules (Figures 2C, 2D). Dentin specimens infiltrated with Zn-NPs attained a 96% of mixed failures (Table 1) and surface analysis exhibited an extended clump of mineral precipitates throughout the dense network of plate-like multilayered crystals on intertubular dentin and at the entrances of some tubules. An extensive labyrinth of anastomoses, cavities and hollows, perceptible at nano-metric scale were also adverted (Figures 2E, 2F).

The second null hypothesis, that calcium and zinc loaded nanoparticles infiltration into the etched dentin does not influence the dynamic mechanical behavior at the hybrid layer, after 21 days of SBFS storage must be rejected, as tan δ increased at the hybrid layer, the bottom of the hybrid layer and intertubular dentin, and decreased at peritubular dentin in specimens treated with Ca-NPs (Table 2) (Figure 4C). On the other hand, storage or elastic modulus (E') (Eq. 8) of dentin samples treated with Ca-NPs diminished, in general, after 21 d of storage in contrast to the group of 24 h (Table 2). A general idea of the behavior of a viscoelastic material can be obtained by the value of the ratio between the loss and the storage modulus (E''/E'). This quotient is represented by tan δ (Espino et al., 2014), being a measure of the ratio of the energy dissipated by the system to the energy stored in the system that enables its elastic recoil. It reflects how well a material can get rid of the energy. The lower tan δ, the greater the proportion of energy available in the system for recoil and/or failure (Espino et al., 2014). As a consequence, a general trend to lower levels of accumulated energies at the interface can be appreciated after 21 days of SBFS storage, when dentin samples are infiltrated with Ca-NPs. This higher tan δ values complied with the increased of the

phosphate peak, after 21 d of SBFS storage, at the bottom of the hybrid layer (~1.14 fold) and at the underlying dentin (~1.15 fold), and concerns with a generalized augmentation of the carbonate peak at the whole interface (Table 3a) (Figs 6A, 6C). Similarly, the mineral to matrix ratio (MMR_P) and crystallinity ($FWHM_P$) also augmented, at the same time point (Tables 3a, 3b), confirming dentin remineralization (Toledano et al., 2016a), which was consistent with the absence of the bottom of the hybrid layer (Figures 7B, 7C). Thereby, the third null hypothesis must be rejected. This mineralization was evidenced as occluded dentinal tubules combined with thick platform of minerals (Figs 2C, 2D), which exhibited some nuclei of highest tan δ values (Figure 4C). Similarly, the increases of peaks at 1340 cm^{-1} (α-helices), after Raman analysis, denoted a greater sensitivity of collagen to molecular orientation, at dentin, in order to enhance further crystallization (Wang et al., 2009). Furthermore, the ratio amide I/amide III raised and Raman CH_2 signal diminished at dentin when samples were treated with Ca-NPs after 21 d of SBFS storage, indicating better organization of collagen with improved conformation of the polypeptide chains and lower immature stage of the dentin substrate, respectively (Vanna et al., 2015; Wang et al., 2009; Xu and Wang, 2011) (Table 4). Nevertheless, $FWHM_C$ of the carbonate band decreased after 21 d, though MMR_C increased (Tables 3a, 3b). Lower $FWHM_P$ denoted, as a result, an improved crystallographic or relative atomic order, since narrower peaks suggest less structural variation in bond distances and angles (Schwartz et al., 2012). In general, the narrower the spectral peak width is, the higher the degree of mineral crystallinity (Karan et al., 2009). If crystalline calcium phosphates are formed, they will have long degradation times, requiring months or even years to provide ions to the remineralizing media (Rezwan et al., 2006).

On the contrary, specimens treated with non-doped NPs and stored 21 d demonstrated lower values of phosphate and carbonate contents, and also lower crystallinity of both phosphate and carbonate groups at the whole interface (Tables 3a, 3b), performing an amorphization process (Toledano et al., 2016c) at the interface, in absence of Ca or Zn chelating/complexing ions. As a consequence, partial remineralization did exist at intertubular and intratubular dentin (Figure 2B) even though the tan δ of the interface was not affected after 21 d of SBFS immersion (Table 2).

In specimens treated with Zn-NPs, tan δ decreased, after 21 days of SBFS storage, at intertubular dentin (Table 2). Furthermore, zones of lower dissipation of energy were created between intertubular and peritubular dentin at both 24 h (0.27 *vs* 0.08 GPa) (Figure 3D) and 21 days (0.20 *vs* 0.07 GPa) of SBFS storage (Table 2). These zones promote stress concentration and breaking with failure of the resin-dentin interface (Angker and Swain, 2006), and concur with areas of unchanged crystallinity (FWHM$_P$), but with lower mineral to matrix ratio (MMR$_P$ and MMR$_C$) (Figures 7A, 7C). Similarly, Raman analysis also exhibited an increase of collagen crosslinking at the hybrid layer and dentin (Table 4), conducting to a less mineralized (Schwartz et al., 2012) but more mature tissue (Sell and Monnier, 1989), in comparison with dentin treated with Zn-NPs/24 h or Ca-NPs/21 d. Collagen crosslinking is affected by the tissue maturation as well as the degree of mineralization, providing information about the structure and molecular interactions of complexes biomolecules (Saito et al., 2006; Xu and Wang, 2011). Pentosidine, is the main AGE (advance glycation end products) component (Salehi et al., 2013). Its presence strongly suggest ribose or ribonucleotide metabolites as precursors (Sell and Monnier, 1989). Pentosidine has been demonstrated to contribute to the age-related stiffening of tissues by cross-linking of the extracellular

matrix, and may serve as a molecular marker of the aging process (Sell and Monnier, 1989). The higher intensity signal at the interface indicates greater potential for further remineralization and scaffolding (Salehi et al., 2013), considering that both hybrid layer and dentin resulted in a more immature substrate (increased CH_2 peak) (Table 4) but with better organization of collagen for promoting apatite nucleation (increased ratio A-I/A-III) (Table 4) (Xu and Wang, 2012). After 24 h of SBFS storage, some demineralized collagen fibers were patent at the bottom of the Zn-NPs-infiltrated hybrid layer, reflecting this lack of complete remineralization (Figures 2E, 2F). Nevertheless, when Ca-NPs were used (Figure 7B) instead of Zn-NPs (Figure 8B) the resin-dentin interface, after 21d of SBFS storage, resulted more homogeneous from a chemical stand point. In both type of interfaces, the bottom of the hybrid layer was absent, due to mineral precipitation (Figures 7C, 8C).

It is worth to stress that specimens treated with Ca-NPs attained higher carbonate content at the hybrid layer than samples treated with Zn-NPs (Table 3b). Similarly, the gradient of mineral content (GMC) also raised in samples treated with Ca-NPs in contrast to Zn-NPs, associated with an increase of amorphous calcium phosphate compounds, *i.e*, an augment of mineralization based on complementary amorphous components was generated. Incorporation of carbonate leads to immature hydroxyapatite. On the whole, the hydroxyapatite with poor crystallinity has improved bioactivity, biocompatibility and biodegradability as compared with the stoichiometric hydroxyapatite. The dissolution of hydroxyapatite increases the level of supersaturation, and thus raises the velocities of nucleation and growth of dentin-like apatite nanocrystals (Chen et al., 2014).

Specimens treated with Zn-NPs, attained an increase of the storage modulus (E') at the intertubular dentin ~1.62 fold, in comparison with the samples stored for 24 h

(Table 2). As stated above, storage modulus represents the elastic energy stored which is released after deformation, characterizing the elastic behavior (Espino et al., 2014; Ryou et al., 2015). Mapping of the bonded interfaces enabled identification of both peritubular and intertubular dentin in the property maps as one of the most crucial junctions in preventing crack generation and propagation across the boundary between the two different phases (Angker and Swain, 2006). Lower storage modulus (E') regions with high flexibility (*e.g*, intertubular dentin in the Zn-NPs group: 85.88 GPa) lead to stress concentration in relatively higher elastic modulus regions, with low flexibility (Gopalakrishnan and Zukoski, 2007) (*e.g,* peritubular dentin: 151 GPa) (Table 2). The ratio peritubular/intertubular dentin concerning E' (1.76) represents the energy stored that would, potentially, be dissipated through cracking the tissue (Misra et al., 2004), *i.e.*, the resin-dentin interface (Figure 4D). This quotient decreased when interfaces were infiltrated with Ca-NPs (1.65), releasing the stress at this location in a more favorable behavior, without producing viscoelastic-related morphological changes at the interface (Figure 5 C).

A measure of the resistance of a material to dynamic deformation or robustness is provided by the value of the complex modulus ($E*$) (Ryou et al., 2013) (Eqs 5, 6). Twenty one days of immersion in SBFS promoted a generalized decrease of $E*$ at the whole structures of the resin-dentin interface when Ca-NPs were used to infiltrate the substrate, except at the adhesive and the hybrid layer that augmented ~1.55 and 1.65 fold, respectively, in contrast to the group stored for 24 h (Table 2). Concerning $E*$ of the specimens treated with Zn-NPs after 21 d of SBFS storage, the resistance of the resin-dentin interface to dynamic deformation augmented at the adhesive and intertubular dentin layers (~2.08 and ~1.76 fold, respectively), in comparison with the specimens stored 24 h (Table 2). Due to the light increase in both peak and area of the

phosphate group and area of the carbonate group (Table 3a), changes in the viscoelastic mechanical behavior are not unexpected (Toledano et al., 2016d). The significance of this finding lies in the weak resistance to deformation that is achieved at dentin, after 21 d of SBFS storage, due to their scarce remineralization (Balooch et al., 2008) when NPs were doped with both Ca and Zn.

Complex modulus correlates with stiffness (Ryou et al., 2013). In general, elastic modulus is not the same as stiffness. Elastic modulus is a property of the constituent material. Stiffness is a property of the structure, *i.e,* the modulus is an intensive or intrinsic property of the material, whereas stiffness is an extensive or extrinsic property of the solid body dependent on the material and the shape and boundary conditions (Gopalakrishnan and Zukoski, 2007). Nano-DMA revealed that there is heterogeneity in the mechanical property distribution of both intertubular and peritubular dentin in the group of 24 h of storage. The nano-DMA analysis of the complex modulus at peritubular dentin in samples treated with Ca-NPs stored for 24 h permitted observation of zones with higher E^* (215.78 GPa) close to areas of lower modulus (116.84 GPa at intertubular dentin, 110.04 GPa at the bottom of the hybrid layer, or 64.34 GPa at the hybrid layer) (Table 2), which might hinder the dissipation of energy through the interface (Agrawal et al., 2013). Low modulus regions lead to stress concentration in relatively high elastic modulus regions (Misra et al., 2004). Thereby, if at the peritubular dentin the energy stored is too great, then excess energy would potentially be dissipated through cracking of the tissue; *i.e.,* resin-dentin interface failure. This mechanism would be consistent with resin-dentin inter-diffusion zone breakdown, preferentially at the limits of the peritubular dentin and the rest of the structures involved at the interface. From the stress distribution mapped by Misra et al. (2004), it can be inferred that failure or fracture could probably initiate at three locations within

the hybrid layer and the dentin: *(i)* at the adhesive tag proximal to the hybrid layer due to stress concentration, *(ii)*, close to the bottom of the hybrid layer due to high strain; and *(iii)* at the interface between the adhesive tag and the peritubular dentin of the lumen wall due to stress concentration (Misra et al., 2005). Furthermore, if the bond between the adhesive tags and peritubular dentin is imperfect, as in Figures 2F and 5D, then the stress concentration zones are probably within the hybrid layer, where stresses will concentrate and the integrity of the resin-dentin interface will get damaged (Toledano et al., 2016d).

When dentin samples were treated with Ca-NPs and Zn-NPs, and stored for 21 d, the *E** percentage of intertubular dentin increased up to ~67% and ~83% respect to the peritubular dentin (Table 2). This growing made that viscoelasticity values at both intertubular and peritubular dentin became homogeneous facilitating, thereby, the dissipation of energy throughout their structures (Agrawal et al., 2013). Even more, the range of discrepant values among the four constituents of the adhesive interface when Ca- or Zn-doped NPs were employed diminished after 21 d of storage, contributing to lower resistance to deformation within the interface after prolonged storage. Similar viscoelastic performance was observed after measuring and comparing *E** at the interface of specimens infiltrated with SB, at 24 h (Figure 3A) and 21 d (Figure 4A) and NPs at 24 h and 21 d (Figure 4B) time points (Table 2). Therefore, the difference of resistance to deformation between intertubular and peritubular dentin was lesser after 21 d than after 24 h of SBFS storage (Table 2), helping for a proper dissipation of energy.

There is a significant scope in the application of nanomaterials to positively interfere in dental caries development and progression. These materials should ideally be able to provide calcium and phosphate ions for improving tooth remineralization, and nanosize will permit these materials to enter through tooth tissue porosities (Souza et

al., 2015). This effect may also be facilitated by the ability of these NPs to inhibit dentin metalloproteinases (Osorio et al., 2014), enzymes implicated in dentinal carious process (Tjäderhane et al., 2015). It has to be ascertained if tested nanoparticles may also offer opportunities to sustain a locally Ca and P-rich environment for the treatment of dental caries. This has potential relevance for the treatment of dental demineralization, instead of using Ca and P delivery conventional materials in which the controlled ions release is controversial. The possibility of incorporating proteins (*e.g.* mineralizing factors, enzymes inhibitors) trough binding or adsorption, will provide more cues to tissue mineralization (Choi et al., 2013). One of the main problems when incorporating calcium and phosphate containing particles into dental adhesives is the control of the calcium and phosphate release kinetic. Tested NPs may overcome this situation, as polymeric NPs do not dissolve or reabsorb, but are able to form amorphous calcium phosphate layer at their surface (Osorio et al., 2016b) and will remain attached to collagen fibrils (Osorio et al., 2014), being incorporated into the remineralized tissue (Figures 2D, 2F). Therefore, NPs will facilitate mineral deposits formation. Carboxylate groups (COOH) may template the growth of calcium phosphates, as it has been previously demonstrated in other different synthetic polymers (Li et al., 2013; Song et al., 2005). If these formed mineral deposits will also facilitate a certain degree of intrafribrillar mineralization deserve future research. However, calcium and phosphate ions seem to be effective in dentin remineralization, where remaining mineral is present (Thompson et al., 2013), as it exists in partially demineralized dentin at the hybrid layer (Song et al., 2005). Although seen from the outside, this work might suffer from the innate drawbacks that doping can affect the properties of the NPs, including size, surface area, crystallinity and solubility and, in turns, this could negate the effect of ions. In addition, the tentative changes in the physicochemical properties of the doped

adhesive should be determined. This can be considered as a study limitation of the present research. Complementary studies, therefore, are required to elucidate in this way.

These are to the best of our knowledge, the solely available results from nano-DMA and Raman analysis experiments on Ca and Zn-doped NPs infiltrating the resin-dentin interface. Future research should also be aimed to morpho-physico-chemically characterize these resin-dentin interfaces through micro-XRD[2], transmission electron microscopy, X-ray micro-computed tomography and X-ray fluorescence microscopy studies.

5. Conclusions

This work proved that ion doping in nanoparticles has a strong impact on resin-dentin interface behavior. Considering bonding efficacy, to incorporate NPs into the adhesive resin do not compromise the bond strength of the adhesive system to dentin. From a viscoelastic point of view, Ca-doping NPs caused an improved and favorable dissipation of energy when compared with Zn-doping NPs. On the other hand, dentin infiltrated with Zn-NPs released the stress by breaking the resin-dentin interface and creating specific mineral formations in response to the energy dissipation. From a chemical perspective, ion-doped NPs contributed to increase the presence of crystalline minerals at the resin-dentin interface in contrast to the non-doped NPs. The presence of Zn-NPs or Ca-NPs at the interface provoked a generalized low-carbonate substitute apatite precipitation at any time of storage, contributing to improve the mechanical performance of the whole resin-dentin interface. All of these findings are foreseen to have great potential, especially Ca-doping NPs, in guiding the design of new NPs with advanced biological and clinical performance.

Acknowledgments

REFERENCES

Ager, J.W., Nalla, R.K., Breeden, K.L., Ritchie, R.O., 2005. Deep-ultraviolet Raman spectroscopy study of the effect of aging on human cortical bone. J. Biomed. Opt. 10, 034012. DOI:10.1117/1.1924668

Agrawal, R., Nieto, A., Chen, H., Mora, M., Agarwal, A., 2013. Nanoscale damping characteristics of boron nitride nanotubes and carbon nanotubes reinforced polymer composites. ACS Appl. Mater. Interfaces 5, 12052–12057. DOI:10.1021/am4038678

Almahdy, A., Downey, F.C., Sauro, S., Cook, R.J., Sherriff, M., Richards, D., Watson, T.F., Banerjee, A., Festy, F., 2012. Microbiochemical analysis of carious dentine using Raman and fluorescence spectroscopy. Caries Res. 46, 432–440. DOI:10.1159/000339487

Angker, L., Swain, M.V., 2006. Nanoindentation: Application to dental hard tissue investigations. J. Mater. Res. 21, 1893–1905. DOI:10.1557/jmr.2006.0257

Balooch, M., Habelitz, S., Kinney, J.H., Marshall, S.J., Marshall, G.W., 2008. Mechanical properties of mineralized collagen fibrils as influenced by demineralization. J. Struct. Biol. 162, 404–410. DOI:10.1016/j.jsb.2008.02.010

Barcellos, D.C., Fonseca, B.M., Pucci, C.R., Cavalcanti, B. das N., Persici, E.D.S., Gonçalves, S.E. de P., 2016. Zn-doped etch-and-rinse model dentin adhesives: Dentin bond integrity, biocompatibility, and properties. Dent. Mater. 32, 940–950. DOI:10.1016/j.dental.2016.04.003

Bar-On, B., Wagner, H.D., 2012. Elastic modulus of hard tissues. J. Biomech. 45, 672–678. DOI:10.1016/j.jbiomech.2011.12.003

Bertassoni, L.E., Habelitz, S., Kinney, J.H., Marshall, S.J., Marshall, G.W., 2009. Biomechanical perspective on the remineralization of dentin. Caries Res. 43, 70–77. DOI:10.1159/000201593

Bertassoni, L.E., Habelitz, S., Pugach, M., Soares, P.C., Marshall, S.J., Marshall, G.W., 2010. Evaluation of surface structural and mechanical changes following remineralization of dentin. Scanning 32, 312–319. DOI:10.1002/sca.20199

Besinis, A., De Peralta, T., Handy, R.D., 2014. The antibacterial effects of silver, titanium dioxide and silica dioxide nanoparticles compared to the dental disinfectant chlorhexidine on Streptococcus mutans using a suite of bioassays. Nanotoxicology 8, 1–16. DOI:10.3109/17435390.2012.742935

Besinis, A., van Noort, R., Martin, N., 2012. Infiltration of demineralized dentin with silica and hydroxyapatite nanoparticles. Dent. Mater. 28, 1012-1023. DOI:10.1016/j.dental.2012.05.007

Besinis, A., van Noort, R., Martin, N., 2016. The use of acetone to enhance the infiltration of HA nanoparticles into a demineralized dentin collagen matrix. Dent. Mater. 32, 385–393. DOI:10.1016/j.dental.2015.11.010

Bonifacio, A., Beleites, C., Vittur, F., Marsich, E., Semeraro, S., Paoletti, S., Sergo, V., 2010. Chemical imaging of articular cartilage sections with Raman mapping, employing uni- and multi-variate methods for data analysis. Analyst 135, 3193–3204. DOI:10.1039/c0an00459f

Breschi, L., Mazzoni, A., Nato, F., Carrilho, M., Visintini, E., Tjäderhane, L., Ruggeri, A., Tay, F.R., Dorigo, E.D.S., Pashley, D.H., 2010. Chlorhexidine stabilizes the adhesive interface: a 2-year in vitro study. Dent. Mater. 26, 320–325. DOI:10.1016/j.dental.2009.11.153

Carrilho, M.R., Tay, F.R., Donnelly, A.M., Agee, K.A., Tjäderhane, L., Mazzoni, A., Breschi, L., Foulger, S., Pashley, D.H., 2009. Host-derived loss of dentin matrix stiffness associated with solubilization of collagen. J. Biomed. Mater. Res. B Appl. Biomater. 90, 373–380. DOI:10.1002/jbm.b.31295

Chen, C., Liu, J., Sun, F., Stansbury, J.W., 2014. Tuning the surface microstructure and gradient properties of polymers by photopolymerizable polysiloxane-modified nanogels. RSC Adv. 4, 28928–28936. DOI:10.1039/C4RA02176B

Choi, W.J., Lee, J.H., Park, M.H., Choi, I.Y., Park, J.K., Shin, J.K., Lee, S.A., Paik, W.Y., Lee, J.H., 2013. Influence of the vitrification solution on the angiogenic factors in vitrificated mouse ovarian tissue. Obstet. Gynecol. Sci. 56, 382–388. DOI:10.5468/ogs.2013.56.6.382

Espino, D.M., Shepherd, D.E.T., Hukins, D.W.L., 2014. Viscoelastic properties of bovine knee joint articular cartilage: dependency on thickness and loading frequency. BMC Musculoskel. Dis. 15, 205. DOI:10.1186/1471-2474-15-205

Gopalakrishnan, V., Zukoski, C.F., 2007. Delayed flow in thermo-reversible colloidal gels. J. Rheol. 51, 623–644. DOI:10.1122/1.2736413

Habelitz, S., Balooch, M., Marshall, S.J., Balooch, G., Marshall, G.W., 2002. In situ atomic force microscopy of partially demineralized human dentin collagen fibrils. J. Struct. Biol. 138, 227–236.

Han, L., Grodzinsky, A.J., Ortiz, C., 2011. Nanomechanics of the Cartilage Extracellular Matrix. Annu. Rev. Mater. Res. 41, 133–168. DOI:10.1146/annurev-matsci-062910-100431

Hashimoto, M., Ohno, H., Sano, H., Kaga, M., Oguchi, H., 2003. In vitro degradation of resin-dentin bonds analyzed by microtensile bond test, scanning and transmission electron microscopy. Biomaterials 24, 3795–3803.

Hayot, C.M., Forouzesh, E., Goel, A., Avramova, Z., Turner, J.A., 2012. Viscoelastic properties of cell walls of single living plant cells determined by dynamic nanoindentation. J. Exp. Bot. 63, 2525–2540. DOI:10.1093/jxb/err428

Hebling, J., Pashley, D.H., Tjäderhane, L., Tay, F.R., 2005. Chlorhexidine arrests subclinical degradation of dentin hybrid layers in vivo. J. Dent. Res. 84, 741–746.

Hertz, H., 1881. The contact of elastic solids. J. Reine Angew. Math. 92, 156-171.

Hoppe, A., Güldal, N.S., Boccaccini, A.R., 2011. A review of the biological response to ionic dissolution products from bioactive glasses and glass-ceramics. Biomaterials 32, 2757–2774. DOI:10.1016/j.biomaterials.2011.01.004

Hu, S., Li, J., Liu, L., Dai, R., Sheng, Z., Wu, X., Feng, X., Yao, X., Liao, E., Keller, E., Jiang, Y., 2015. Micro/Nanostructures and Mechanical Properties of Trabecular Bone in Ovariectomized Rats. Int. J. Endocrinol. 252503. DOI:10.1155/2015/252503

Jastrzebska, M., Wrzalik, R., Kocot, A., Zalewska-Rejdak, J., Cwalina, B., 2003. Raman spectroscopic study of glutaraldehyde-stabilized collagen and pericardium tissue. J. Biomat. Sci-Polym. E. 14, 185–197.

Karan, K., Yao, X., Xu, C., Wang, Y., 2009. Chemical profile of the dentin substrate in non-carious cervical lesions. Dent. Mater. 25, 1205–1212. DOI:10.1016/j.dental.2009.04.006

Kokubo, T., Kushitani, H., Sakka, S., Kitsugi, T., Yamamuro, T., 1990. Solutions able to reproduce in vivo surface-structure changes in bioactive glass-ceramic A-W3. J. Biomed. Mater. Res. 24, 721–734. DOI:10.1002/jbm.820240607

Kunstar, A., Leijten, J., van Leuveren, S., Hilderink, J., Otto, C., van Blitterswijk, C.A., Karperien, M., van Apeldoorn, A.A., 2012. Recognizing different tissues in

human fetal femur cartilage by label-free Raman microspectroscopy. J. Biomed. Opt. 17, 116012. DOI:10.1117/1.JBO.17.11.116012

Li, J., Yang, J., Li, J., Chen, L., Liang, K., Wu, W., Chen, X., Li, J., 2013. Bioinspired intrafibrillar mineralization of human dentine by PAMAM dendrimer. Biomaterials 34, 6738–6747. DOI:10.1016/j.biomaterials.2013.05.046

Li, Y., Thula, T.T., Jee, S., Perkins, S.L., Aparicio, C., Douglas, E.P., Gower, L.B., 2012. Biomimetic mineralization of woven bone-like nanocomposites: role of collagen cross-links. Biomacromolecules 13, 49–59. DOI:10.1021/bm201070g

Liu, Y., Yao, X., Liu, Y.W., Wang, Y., 2014. A Fourier transform infrared spectroscopy analysis of carious dentin from transparent zone to normal zone. Caries Res. 48, 320–329. DOI:10.1159/000356868

Lynch, R.J.M., Churchley, D., Butler, A., Kearns, S., Thomas, G.V., Badrock, T.C., Cooper, L., Higham, S.M., 2011. Effects of zinc and fluoride on the remineralisation of artificial carious lesions under simulated plaque fluid conditions. Caries Res. 45, 313–322. DOI:10.1159/000324804

Macosko, C.W. 1994. Rheology: Principles, Measurements, and Applications. VCH Publishers, New York.

Marshall, G.W., Habelitz, S., Gallagher, R., Balooch, M., Balooch, G., Marshall, S.J., 2001. Nanomechanical properties of hydrated carious human dentin. J. Dent. Res. 80, 1768–1771.

Mayer, I., Apfelbaum, F., Featherstone, J.D., 1994. Zinc ions in synthetic carbonated hydroxyapatites. Arch. Oral Biol. 39, 87–90.

Medina-Castillo AL, Fernandez-Sanchez JF, Segura-Carretero A, Fernandez-Gutierrez A., 2010. Micrometer and submicrometer particles prepared by precipitation polymerization: thermodynamic model and experimental evidence of the relation

between Flory's parameter and particle size. Macromolecules 43, 5804–5813. DOI: 10.1021/ma100841c

Milly, H., Festy, F., Watson, T.F., Thompson, I., Banerjee, A., 2014. Enamel white spot lesions can remineralise using bio-active glass and polyacrylic acid-modified bio-active glass powders. J. Dent. 42, 158–166. DOI:10.1016/j.jdent.2013.11.012

Misra, A., Spencer, P., Marangos, O., Wang, Y., Katz, J.L., 2004. Micromechanical analysis of dentin/adhesive interface by the finite element method. J. Biomed. Mater. Res. B Appl. Biomater. 70, 56–65. DOI:10.1002/jbm.b.30012

Misra, A., Spencer, P., Marangos, O., Wang, Y., Katz, J.L., 2005. Parametric study of the effect of phase anisotropy on the micromechanical behaviour of dentin-adhesive interfaces. J. Roy. Soc. Interface 2, 145–157. DOI:10.1098/rsif.2005.0029

Nakabayashi, N., Pashley, D.H., 1998. Hybridization of Dental Hard Tissues. Quintessence Publishing Co. Ltd., Tokyo.

Osorio, R., Alfonso-Rodríguez, C.A., Medina-Castillo, A.L., Alaminos, M., Toledano, M., 2016b. Bioactive polymeric nanoparticles for periodontal therapy. PloS One 11, e0166217. DOI:10.1371/journal.pone.0166217

Osorio, R., Cabello, I., Medina-Castillo, A.L., Osorio, E., Toledano, M., 2016a. Zinc-modified nanopolymers improve the quality of resin-dentin bonded interfaces. Clin. Oral Investig 20, 2411-2420. DOI:10.1007/s00784-016-1738-y

Osorio, R., Osorio, E., Medina-Castillo, A.L., Toledano, M., 2014. Polymer nanocarriers for dentin adhesion. J. Dent. Res. 93, 1258–1263. DOI:10.1177/0022034514551608

Osorio, R., Yamauti, M., Osorio, E., Román, J.S., Toledano, M., 2011. Zinc-doped dentin adhesive for collagen protection at the hybrid layer. Eur. J. Oral Sci. 119, 401–410. DOI:10.1111/j.1600-0722.2011.00853.x

Pashley, D.H., Tay, F.R., Yiu, C., Hashimoto, M., Breschi, L., Carvalho, R.M., Ito, S., 2004. Collagen degradation by host-derived enzymes during aging. J. Dent. Res. 83, 216–221.

Poon, B., Rittel, D., Ravichandran, G., 2008. An analysis of nanoindentation in linearly elastic solids. Int. J. Solids Struct. 45, 6018–6033. DOI:10.1016/j.ijsolstr.2008.07.021

Prati, C., Chersoni, S., Pashley, D.H., 1999. Effect of removal of surface collagen fibrils on resin-dentin bonding. Dent. Mater. 15, 323–331.DOI:10.1016/S0109-5641(99)00052-4

Profeta, A.C., 2014. Dentine bonding agents comprising calcium-silicates to support proactive dental care: Origins, development and future. Dent. Mater. J. 33, 443–452. DOI:10.4012/dmj.2013-267

Rettler, E., Hoeppener, S., Sigusch, B.W., Schubert, U.S., 2013. Mapping the mechanical properties of biomaterials on different length scales: depth-sensing indentation and AFM based nanoindentation. J. Mater. Chem. B 1, 2789–2806. DOI:10.1039/C3TB20120A

Rezwan, K., Chen, Q.Z., Blaker, J.J., Boccaccini, A.R., 2006. Biodegradable and bioactive porous polymer/inorganic composite scaffolds for bone tissue engineering. Biomaterials 27, 3413–3431. DOI:10.1016/j.biomaterials.2006.01.039

Ryou, H., Pashley, D.H., Tay, F.R., Arola, D., 2013. A characterization of the mechanical behavior of resin-infiltrated dentin using nanoscopic Dynamic

Mechanical Analysis. Dent. Mater. 29, 719–728. DOI:10.1016/j.dental.2013.03.022

Ryou, H., Romberg, E., Pashley, D.H., Tay, F.R., Arola, D., 2015. Importance of age on the dynamic mechanical behavior of intertubular and peritubular dentin. J. Mech. Behav. Biomed. Mater. 42, 229–242. DOI:10.1016/j.jmbbm.2014.11.021

Saito, M., Fujii, K., Marumo, K., 2006. Degree of mineralization-related collagen crosslinking in the femoral neck cancellous bone in cases of hip fracture and controls. Calcif. Tissue Int. 79, 160–168. DOI:10.1007/s00223-006-0035-1

Salehi, H., Terrer, E., Panayotov, I., Levallois, B., Jacquot, B., Tassery, H., Cuisinier, F., 2013. Functional mapping of human sound and carious enamel and dentin with Raman spectroscopy. J. Biophotonics 6, 765–774. DOI:10.1002/jbio.201200095

Sauro, S., Osorio, R., Osorio, E., Watson, T.F., Toledano, M., 2013. Novel light-curable materials containing experimental bioactive micro-fillers remineralise mineral-depleted bonded-dentine interfaces. J. Biomat. Sci-Polym. Ed. 24, 940–956. DOI:10.1080/09205063.2012.727377

Schwartz, A.G., Pasteris, J.D., Genin, G.M., Daulton, T.L., Thomopoulos, S., 2012. Mineral distributions at the developing tendon enthesis. PloS One 7, e48630. DOI:10.1371/journal.pone.0048630

Sell, D.R., Monnier, V.M., 1989. Structure elucidation of a senescence cross-link from human extracellular matrix. Implication of pentoses in the aging process. J. Biol. Chem. 264, 21597–21602.

Song, J., Malathong, V., Bertozzi, C.R., 2005. Mineralization of synthetic polymer scaffolds: a bottom-up approach for the development of artificial bone. J. Am. Chem. Soc. 127, 3366–3372. DOI:10.1021/ja043776z

Song, J., Ugai, H., Nakata-Tsutsui, H., Kishikawa, S., Suzuki, E., Murata, T., Yokoyama, K.K., 2003. Transcriptional regulation by zinc-finger proteins Sp1 and MAZ involves interactions with the same cis-elements. Int. J. Mol. Med. 11, 547–553. DOI: 10.3892/ijmm.11.5.547

Souza, M.A., Oliveira, J.E., Medeiros, E.S., Glenn, G.M., Mattoso, L.H.C., 2015. Controlled release of linalool using nanofibrous membranes of poly(lactic acid) obtained by electrospinning and solution blow spinning: a comparative study. J. Nanosci. Nanotechnol. 15, 5628–5636.

Takatsuka, T., Tanaka, K., Iijima, Y., 2005. Inhibition of dentine demineralization by zinc oxide: in vitro and in situ studies. Dent. Mater. 21, 1170–1177. DOI:10.1016/j.dental.2005.02.006

Thompson, V.P., Watson, T.F., Marshall, G.W., Blackman, B.R.K., Stansbury, J.W., Schadler, L.S., Pearson, R.A., Libanori, R., 2013. Outside-the-(cavity-prep)-box thinking. Adv. Dent. Res. 25, 24–32. DOI:10.1177/0022034513502207

Tjäderhane, L., Buzalaf, M.A.R., Carrilho, M., Chaussain, C., 2015. Matrix metalloproteinases and other matrix proteinases in relation to cariology: the era of "dentin degradomics." Caries Res. 49, 193–208. DOI:10.1159/000363582

Toledano, M., Aguilera, F.S., Osorio, E., Lopez-Lopez, M.T., Cabello, I., Toledano-Osorio, M., Osorio, R., 2016c. Submicron-to-nanoscale structure characterization and organization of crystals in dentin bioapatites. RSC Adv. 6, 45265–45278. DOI:10.1039/C6RA02373H

Toledano, M., Aguilera, F.S., Osorio, E., López-López, M.T., Cabello, I., Toledano-Osorio, M., Osorio, R., 2015. On modeling and nanoanalysis of caries-affected dentin surfaces restored with Zn-containing amalgam and in vitro oral function. Biointerphases 10, 041004. DOI:10.1116/1.4933243

Toledano, M., Aguilera, F.S., Yamauti, M., Ruiz-Requena, M.E., Osorio, R., 2013b. In vitro load-induced dentin collagen-stabilization against MMPs degradation. J. Mech. Behav. Biomed. Mater. 27, 10–18. DOI:10.1016/j.jmbbm.2013.06.002

Toledano, M., Osorio, E., Aguilera, F. S., Cabello, I., Toledano-Osorio, M., Osorio, R., 2016b. *Ex vivo* detection and characterization of remineralized carious dentin, by nanoindentation and single point Raman spectroscopy, after amalgam restoration. J. Raman Spectrosc. *In press.* DOI: 10.1002/jrs.5055.

Toledano, M., Osorio, E., Cabello, I., Aguilera, F.S., López-López, M.T., Toledano-Osorio, M., Osorio, R., 2016d. Nanoscopic dynamic mechanical analysis of resin-infiltrated dentine, under in vitro chewing and bruxism events. J. Mech. Behav. Biomed. Mater. 54, 33–47. DOI:10.1016/j.jmbbm.2015.09.003

Toledano, M., Osorio, R., 2015. New Advanced Materials for High Performance at the Resin-Dentine Interface, in: Deb, S. (Ed.), Biomaterials for Oral and Craniomaxillofacial Applications. Frontiers of Oral Biology. Basel, Karger, London, pp. 39-48.

Toledano, M., Osorio, R., Albaladejo, A., Aguilera, F.S., Tay, F.R., Ferrari, M., 2006. Effect of cyclic loading on the microtensile bond strengths of total-etch and self-etch adhesives. Oper. Dent. 31, 25–32. DOI:10.2341/04-161

Toledano, M., Osorio, R., Osorio, E., García-Godoy, F., Toledano-Osorio, M., Aguilera, F.S., 2016a. Advanced zinc-doped adhesives for high performance at the resin-carious dentin interface. J. Mech. Behav. Biomed. Mater. 62, 247–267. DOI:10.1016/j.jmbbm.2016.05.013

Toledano, M., Sauro, S., Cabello, I., Watson, T., Osorio, R., 2013a. A Zn-doped etch-and-rinse adhesive may improve the mechanical properties and the integrity at

the bonded-dentin interface. Dent. Mater. 29, e142-152. DOI:10.1016/j.dental.2013.04.024

Vanna, R., Ronchi, P., Lenferink, A.T.M., Tresoldi, C., Morasso, C., Mehn, D., Bedoni, M., Picciolini, S., Terstappen, L.W.M.M., Ciceri, F., Otto, C., Gramatica, F., 2015. Label-free imaging and identification of typical cells of acute myeloid leukaemia and myelodysplastic syndrome by Raman microspectroscopy. Analyst 140, 1054–1064. DOI:10.1039/c4an02127d

Vasant, S.R., Joshi, M.J., 2011. Synthesis and characterization of pure and zinc doped calcium pyrophosphate dihydrate nanoparticles. Eur Phys J Appl Phys 53. DOI:10.1051/epjap/2010100095

Wang, C., Wang, Y., Huffman, N.T., Cui, C., Yao, X., Midura, S., Midura, R.J., Gorski, J.P., 2009. Confocal laser Raman microspectroscopy of biomineralization foci in UMR 106 osteoblastic cultures reveals temporally synchronized protein changes preceding and accompanying mineral crystal deposition. J. Biol. Chem. 284, 7100–7113. DOI:10.1074/jbc.M805898200

Wang, Y., Spencer, P., 2003. Hybridization efficiency of the adhesive/dentin interface with wet bonding. J. Dent. Res. 82, 141–145.

Wilkinson, T.M., Zargari, S., Prasad, M., Packard, C.E., 2015. Optimizing nano-dynamic mechanical analysis for high-resolution, elastic modulus mapping in organic-rich shales. J. Mater. Sci. 50, 1041–1049. DOI:10.1007/s10853-014-8682-5

Wu, C., Zhang, Y., Fan, W., Ke, X., Hu, X., Zhou, Y., Xiao, Y., 2011. $CaSiO_3$ microstructure modulating the in vitro and in vivo bioactivity of poly(lactide-co-glycolide) microspheres. J. Biomed. Mater. Res. A 98, 122–131. DOI:10.1002/jbm.a.33092

Xu, C., Wang, Y., 2011. Cross-linked demineralized dentin maintains its mechanical stability when challenged by bacterial collagenase. J. Biomed. Mater. Res. B Appl. Biomater. 96, 242–248. DOI:10.1002/jbm.b.31759

Xu, C., Wang, Y., 2012. Chemical composition and structure of peritubular and intertubular human dentine revisited. Arch. Oral Biol. 57, 383–391. DOI:10.1016/j.archoralbio.2011.09.008

Zhao, X., Shang, T., Zhang, X., Ye, T., Wang, D., Rei, L., 2016. Passage of magnetic Tat-conjugated $Fe_3O_4@SiO_2$ nanoparticles across in vitro blood-brain barrier. Nanoscale Res. Lett. 11, 451. DOI:10.1186/s11671-016-1676-2

FIGURE 1
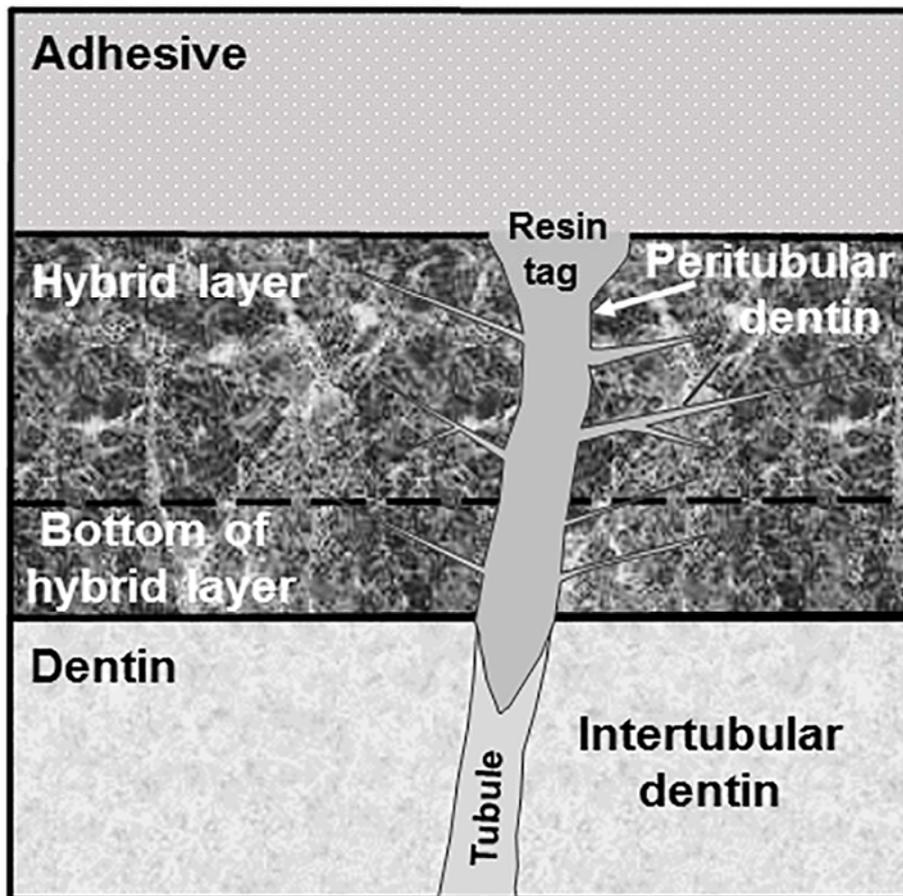
Figure 1. Schematic illustration of the resin-dentin interface. HL: Hybrid Layer; BHL: Bottom of Hybrid Layer; PD: Peritubular Dentin; ID: Intertubular Dentin; rt: resin tag; T: dentinal tubule.

FIGURE 2
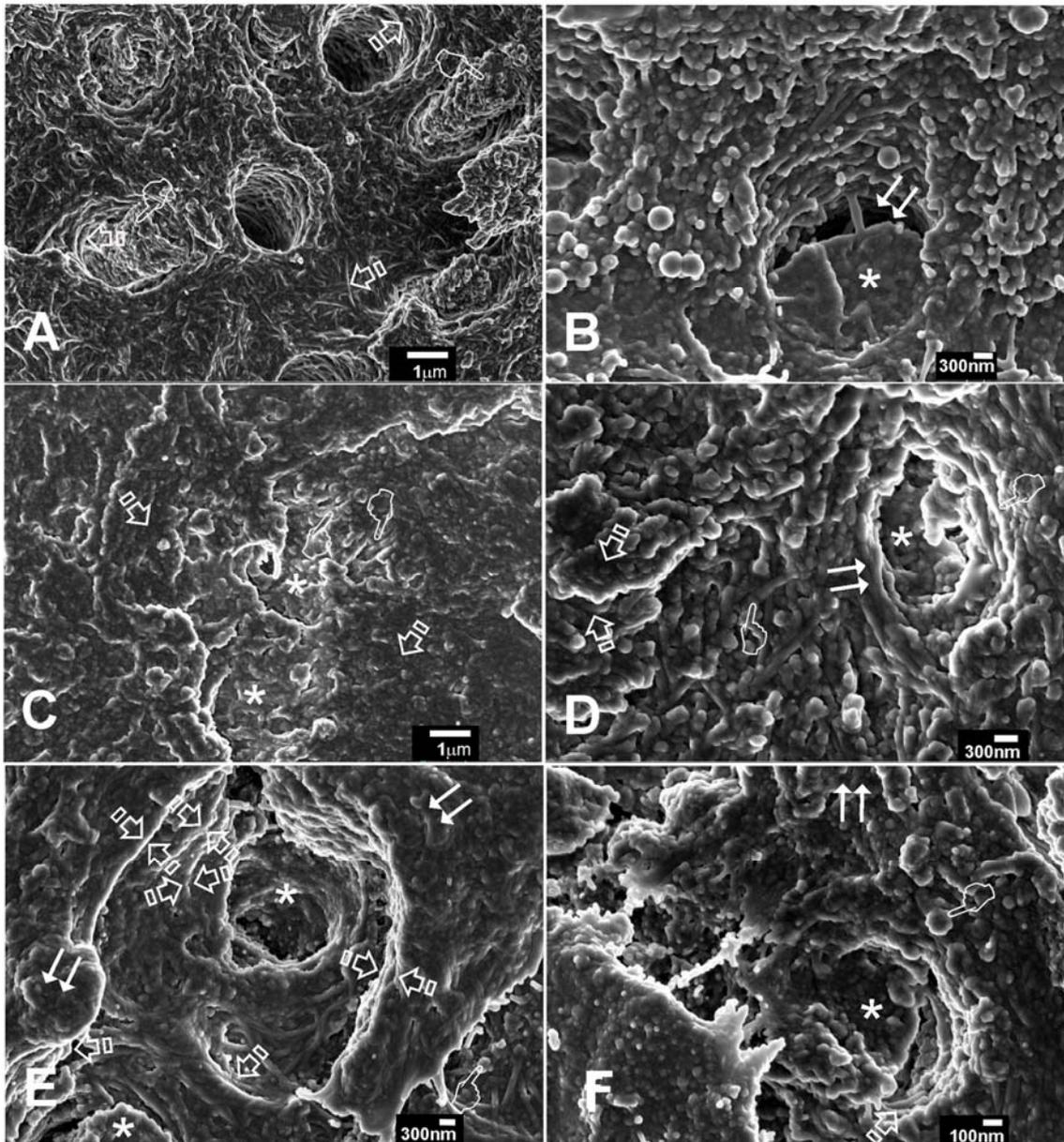
Figure 2. FESEM images of debonded dentin surfaces after microtensile bond strength testing. **A,** failure at the bottom of the hybrid layer when the etched dentin was infiltrated with SB may be shown. Non-resin covered collagen is observed (arrows) and only some resin tags are filling, but not occluding, the dentinal tubules (pointers). **B,** When NPs were applied before bonding with SB, failures at the bottom of the hybrid layer occurred, and NPs remained embedded at the hybrid layer and were

homogeneously distributed on the underlying dentin surface. NPs did not agglomerate, and penetrated dentin tubules, as resin tag constituents (asterisk). Some tubules turned up, thereby, mineral filled but without hermetic sealing (double arrows). Collagen fibers are organized, exhibiting diameters and characteristics periodic striation (pointer). **C, D,** When Ca-NPs were infiltrated in etched dentin before SB application, it was not possible to encounter demineralized collagen fibers or open dentinal tubules, showing intertubular (arrows) and intratubular (asterisks) mineral precipitation. Hybrid layer and mineralized collagen (pointers) were evidenced. Total mineral occlusion of tubules were attained. Minerals formed a collar around the tubule lumen, close by a thick platform of minerals (double arrows). **E, F,** At specimens in which Zn-NPs were applied on etched dentin, tubular occlusion was observed (asterisks), but some demineralized collagen fibers were patent at the bottom of the hybrid layer (arrows). Nanoparticles are hardly distinguished (pointers). Multiple amorphous clumps (double arrows) and multilayered precipitation of minerals, in platforms (faced arrows), appeared covering the intertubular dentin surface growing toward the entrance of tubules, which resulted partially and imperfectly covered.
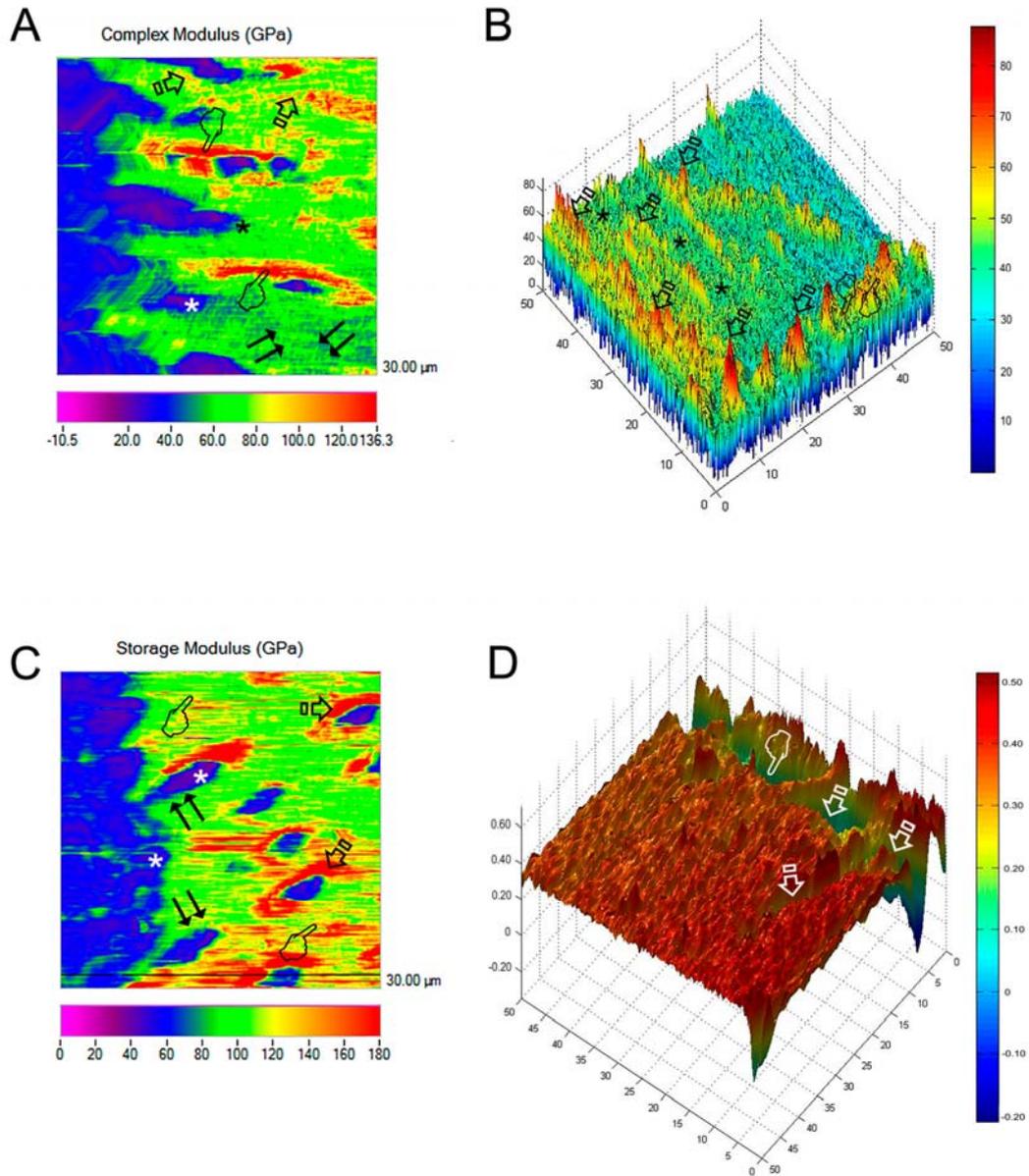
FIGURE 3

Figure 3. A, Scanning mode nano-DMA analysis of the map of the complex modulus/E^* (A), at the SB resin/24 h group. In the color scheme shown, the redder color corresponds to higher values of the locally measured moduli. Interconnected and non-regular yellow color point out areas of E^* associated with intertubular dentin (arrows). The maximum complex modulus became linked to the redder areas, potentially associated to peritubular mineralization (pointers) (A). The hybrid layer was

represented, at the mapping, by the greenish blue fringe (asterisks), and the bottom of the hybrid layer appeared in bluish green (double arrows). **B**, 3-D contour map of the storage modulus (E') distribution in a specimen at the NPs+resin/24 h group. In the color scheme shown, the redder color corresponds to higher values of the locally measured moduli. Peritubular dentin (arrows) showed the biggest elastic behavior (E') as shown in the redder areas, meanwhile both intertubular dentin (asterisks) and hybrid layer (pointers) achieved similar values of E', as shown in the red-yellowish zones. Magnitudes of X, Y and Z axis are in microns. **C,** Scanning mode nano-DMA analysis of the map the storage modulus/E', at the Ca-NPs+resin/24 h group. In the color scheme shown, the redder color corresponds to higher values of the locally measured moduli. Wider pseudo-elliptical circles of higher storage modulus, represented in red are unveiled (arrows), corresponding to the peritubular dentin. They are immersed in an extended area of a lower E', represented at the mapping in yellow (pointers), corresponding with the intertubular dentin. The hybrid layer and the bottom of the hybrid layer appear in blue (asterisks) and green (double arrows), respectively. **D,** 3-D contour map of the tan δ distribution in a specimen at the Zn-NPs+resin/24 h group. In the color scheme shown, the redder color corresponds to higher values of the locally measured moduli. At the resin-dentin inter-diffusion zone, tan δ ranged from 0.08 (peritubular dentin) to 0.27 (intertubular dentin), creating a zone of lower dissipation of energy, and thereby promoting stress concentration and breaking with failure of the resin-dentin interface (arrows). Failure and fracture was also located between the bottom of the hybrid layer (0.19) and the peritubular dentin (pointers), where stresses and energies were concentrated and accumulated. Magnitudes of X, Y and Z axis are in microns.
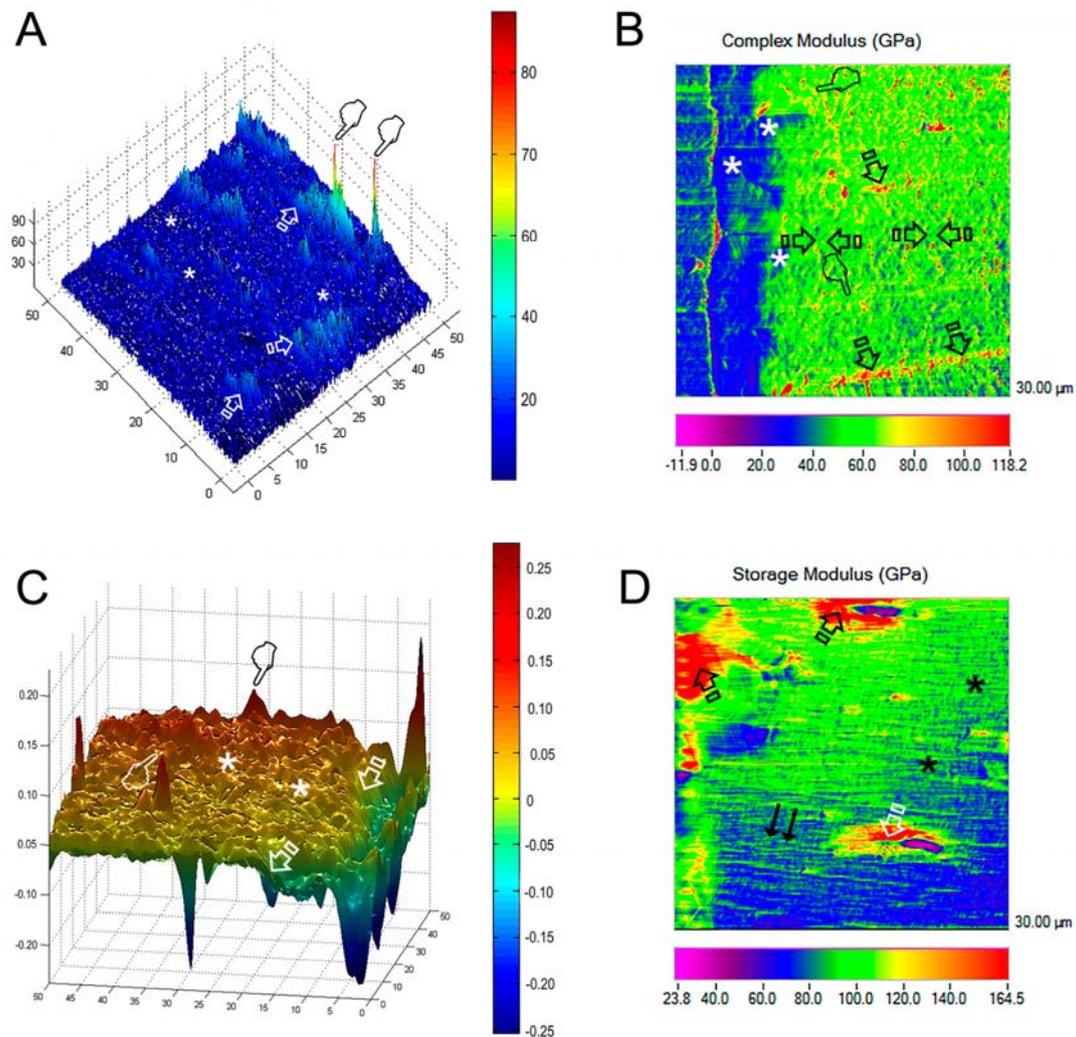
FIGURE 4

Figure 4. **A,** 3-D contour map of the complex modulus/*E** at the SB resin/21 d group. In the color scheme shown, the redder color corresponds to higher values of the locally measured moduli. The mapping reflects regular and continuous rings of moderate complex modulus (arrows), which correspond with the resistance to deformation of peritubular dentin. Very limited areas of high values (pointers) may also be adverted. Intertubular dentin exhibits roughly the half of the values of *E** corresponding to peritubular detin (asterisks). **B,** Scanning mode nano-DMA analysis of the map of the

complex modulus/E^* (A), at the NPs+resin/21 d group. In the color scheme shown, the redder color corresponds to higher values of the locally measured moduli, likely corresponding to the bigger resistance to deformation of the intratubular content (arrows). E^* referred to intertubular and peritubular dentin appear in yellow (pointers) and yellowish green (faced arrows). Both hybrid layer and bottom of hybrid layer are represented by the greenish blue color (asterisks). **C,** 3-D contour map of the tan δ distribution in a specimen at the Ca-NPs+resin/21 d. In the color scheme shown, the redder color corresponds to higher values of the locally measured moduli. At the resin-dentin inter-diffusion zone, tan δ ranged from 0.07 GPa (adhesive) to 0.22 (intertubular dentin). Intertubular dentin (asterisks), approximately, doubled the tan δ values achieved by the peritubular dentin (0.10 GPa) (arrows), creating a zone of stress concentration at this junction. Some nuclei of highest tan δ values were observed at intertubular locations (pointers), probably corresponding with areas of precipitated minerals. Magnitudes of X, Y and Z axis of Figures E and F are in microns. **D,** Scanning mode nano-DMA analysis of the map the storage modulus/E', at the Zn-NPs+resin/21 d group. In the color scheme shown, the redder color corresponds to higher values of the locally measured moduli. It became associated to the elastic energy released, at the peritubular dentin, after deformation; partial redder rings and nodules represented the viscoelastic behavior of this histologic substrate (arrows). The bluish green area identified E' of intertububular dentin (asterisks). The hybrid layer and bottom of the hybrid layer were represented in the greenish blue regions (double arrows).
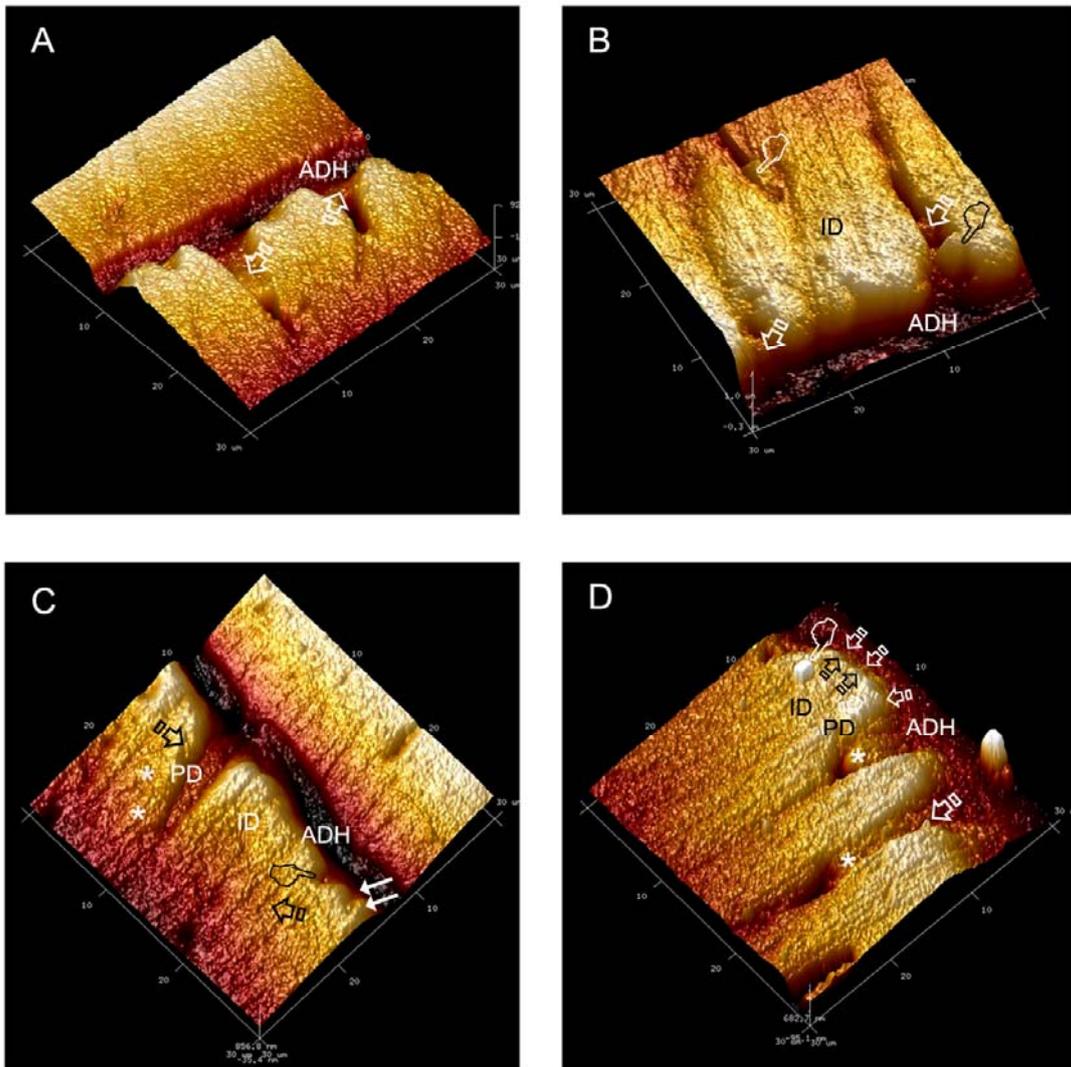
FIGURE 5

Figure 5. A, Topography mapping of the resin-dentin bonded interface obtained by AFM after applying SB, and 24 h in SBFS immersion. Note the adhesive (ADH) forming the partially-infiltrated resin tags within the dentinal tubules (arrows). **B,** Topography mapping of the resin-infiltrated dentin obtained by AFM after applying NPs, 24 h in SBFS immersion. The adhesive (ADH) partially penetrated the dentinal tubules (arrows), and some of them also appeared mineral filled (pointers). Homogenized intertubular (ID) dentin characterized this interface, as zones-free from

breakdown were observed at any location. **C**, Topography mapping of resin-infiltrated dentin obtained by AFM after applying Ca-NPs, and 21 d in SBFS immersion. Strong processes of intertubular and peritubular mineralization are observed (arrows). Firm partial (pointers) or total (double arrows) tubular occlusion is shown. A zone of stress concentration was generated at the junction between peritubular and intertubular dentin (asterisks). **D,** Topography mapping of infiltrated dentin obtained by AFM after applying Zn-NPs and 21 d storing in SBFS. Peritubular (arrow) and intertubular (pointer) mineralization is evident. Resin tags are not occluding totally the dentinal tubules (asterisks). Stick-slip images and little rod-like minerals (faced arrows), as bridge-like structures as sight of energy dissipation maintained anchored the adhesive (ADH) to both peritubular (PD) and intertubular dentin (ID).
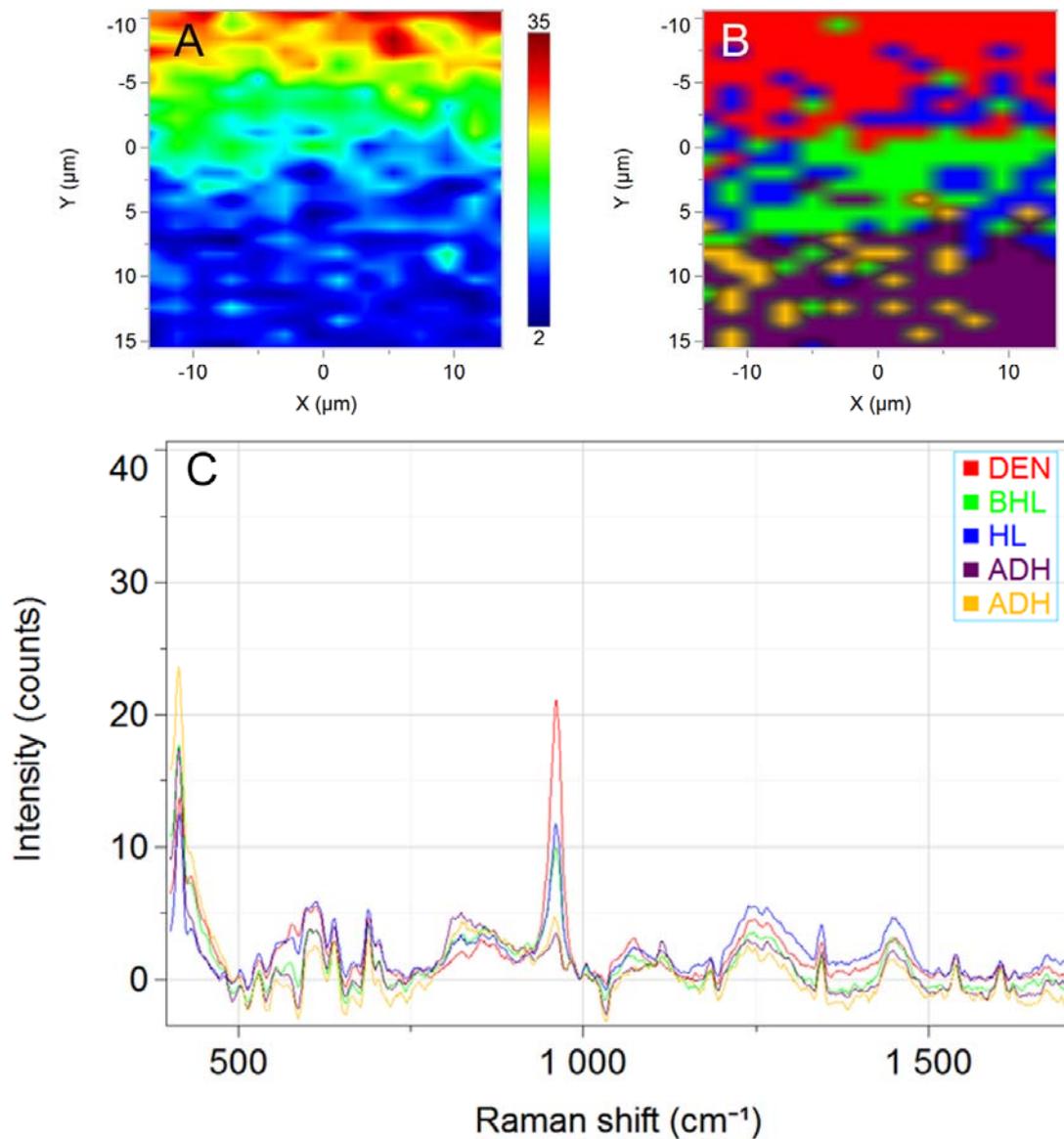
FIGURE 6

Figure 6. 2D micro-Raman map of the phosphate peak (961 cm⁻¹) intensities at the dentin bonded interface infiltrated with SB adhesive and stored in SBFS for 21 days. **B**, K-means clustering (KMC) map of the Raman profile of the sample **C**, Raman *spectra* of principal components (PCs). Abbreviations: ADH, adhesive; HL, hybrid layer; BHL, bottom of hybrid layer; DEN, dentin.
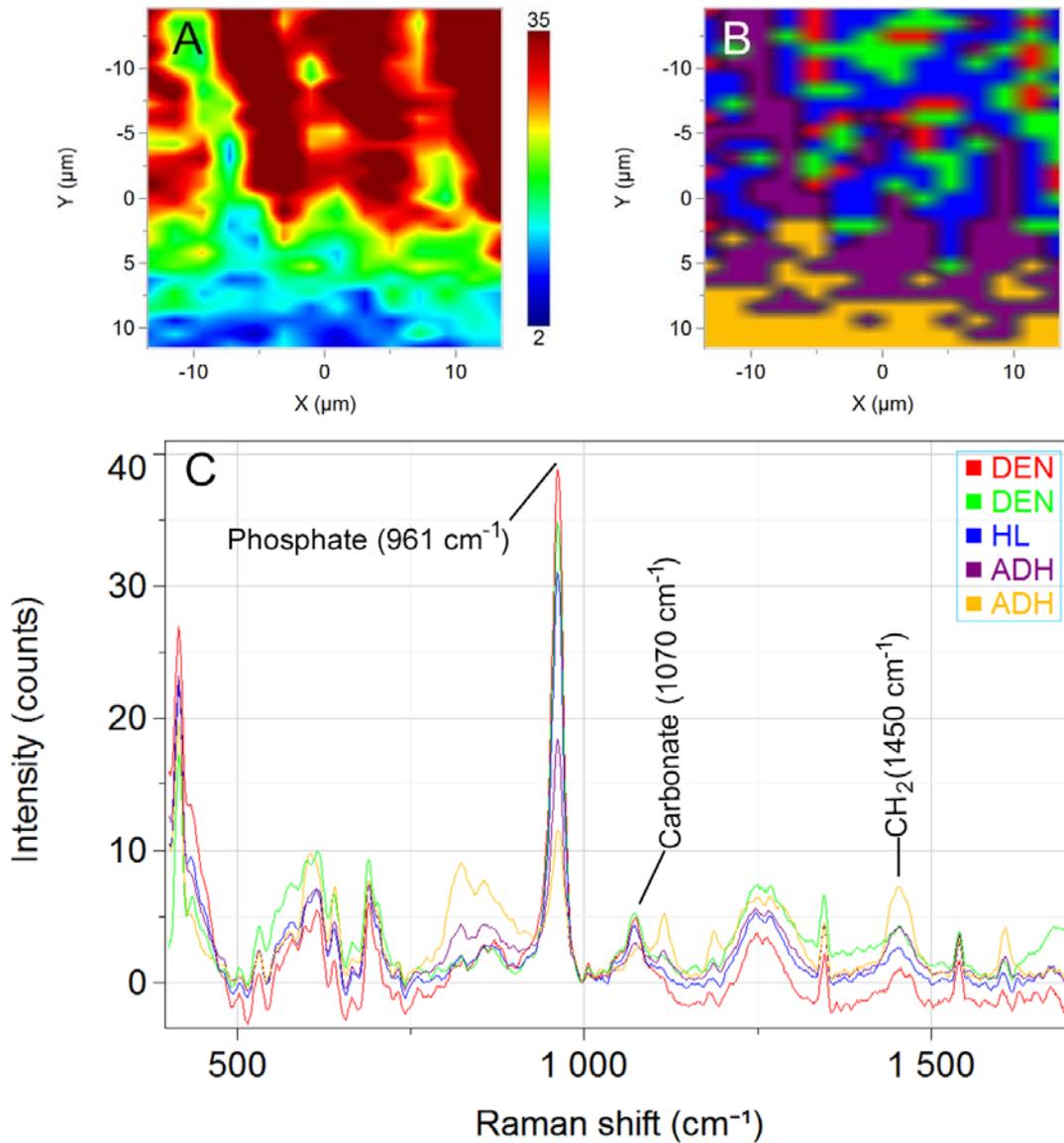
FIGURE 7

Figure 7. A, 2D micro-Raman map of the phosphate peak (961 cm^{-1}) intensities at the dentin bonded interface infiltrated with Ca-NPs, and stored in SBFS for 21 days. B, K-means clustering (KMC) map of the Raman profile of the sample C, Raman *spectra* of principal components (PCs). Abbreviations: ADH, adhesive; HL, hybrid layer; DEN, dentin.
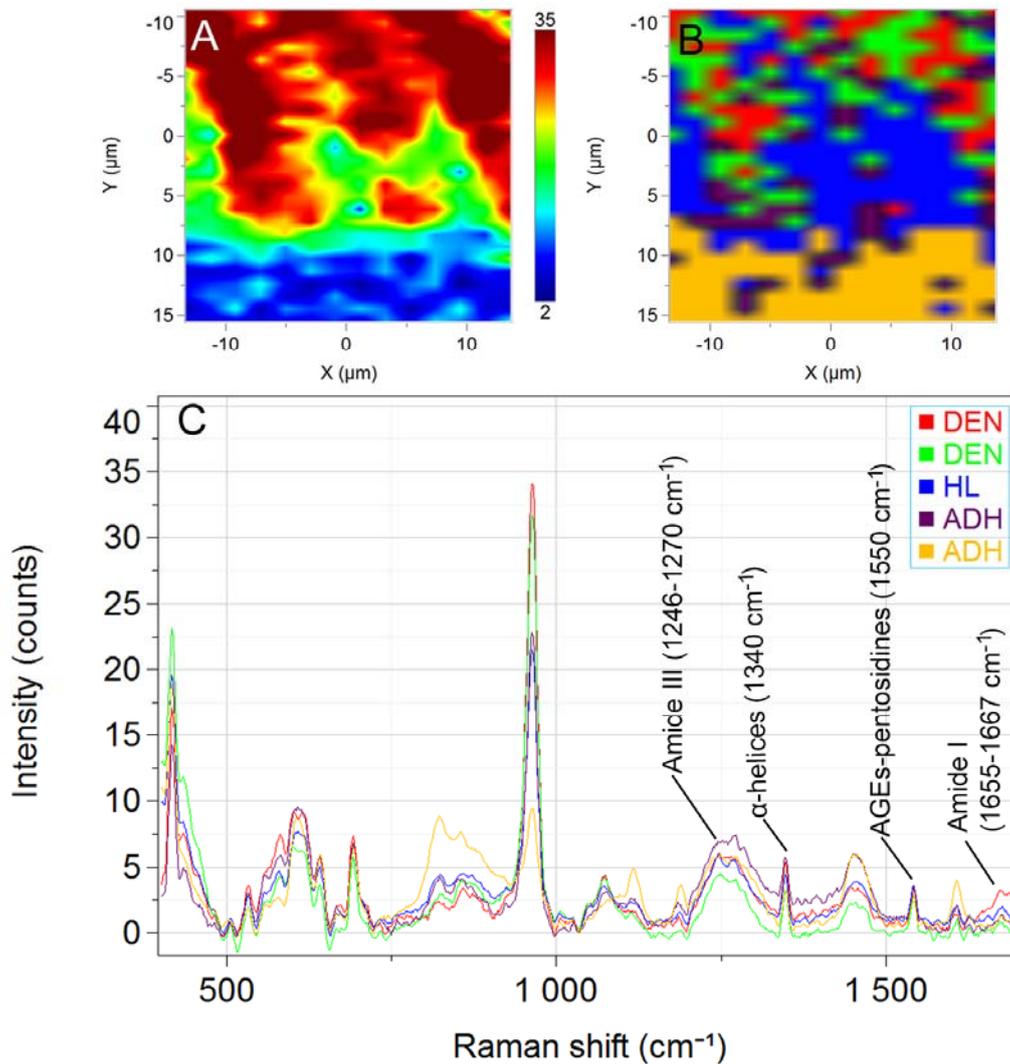
FIGURE 8

Figure 8. A, 2D micro-Raman map of the phosphate peak (961 cm^{-1}) intensities at the dentin bonded interface infiltrated with Zn-NPs, and stored in SBFS for 21 days. **B**, K-means clustering (KMC) map of the Raman profile of the sample **C**, Raman *spectra* of principal components (PCs). Abbreviations: ADH, adhesive; HL, hybrid layer; DEN, dentin.